DENSITY FUNCTIONAL THEORY INVESTIGATION OF THE REACTION MECHANISMS FOR SELECTIVE OXIDATION OF ALCOHOLS ON GOLD CATALYSTS

A THESIS SUBMITTED TO
THE GRADUATE SCHOOL OF NATURAL AND APPLIED SCIENCES
OF
MIDDLE EAST TECHNICAL UNIVERSITY

OZAN DERNEK

IN PARTIAL FULFILLMENT OF THE REQUIREMENTS
FOR
THE DEGREE OF MASTER OF SCIENCE
IN
PHYSICS

SEPTEMBER 2016

Approval of the thesis:

DENSITY FUNCTIONAL THEORY INVESTIGATION OF THE REACTION MECHANISMS FOR SELECTIVE OXIDATION OF ALCOHOLS ON GOLD CATALYSTS

submitted by **OZAN DERNEK** in partial fulfillment of the requirements for the degree of **Master of Science in Physics Department, Middle East Technical University** by,

Prof. Dr. Gülbin Dural Ünver _____
Dean, Graduate School of **Natural and Applied Sciences**

Prof. Dr. Sadi Turgut _____
Head of Department, **Physics**

Assoc. Prof. Dr. Hande Toffoli _____
Supervisor, **Physics Department, METU**

Examining Committee Members:

Prof. Dr. Sadi Turgut
Physics Department, METU _____

Assoc. Prof. Dr. Hande Toffoli
Physics Department, METU _____

Assoc. Prof. Dr. Alpan Bek
Physics Department, METU _____

Assoc. Prof. Dr. Rengin Peköz
Physics Department, Atılım University _____

Assoc. Prof. Dr. Emre Taşçı
Physics Engineering Department, Hacettepe University _____

Date: _____

I hereby declare that all information in this document has been obtained and presented in accordance with academic rules and ethical conduct. I also declare that, as required by these rules and conduct, I have fully cited and referenced all material and results that are not original to this work.

Name, Last Name: OZAN DERNEK

Signature :

ABSTRACT

DENSITY FUNCTIONAL THEORY INVESTIGATION OF THE REACTION MECHANISMS FOR SELECTIVE OXIDATION OF ALCOHOLS ON GOLD CATALYSTS

Dernek, Ozan
M.S., Department of Physics
Supervisor : Assoc. Prof. Dr. Hande Toffoli

September 2016, 49 pages

Most alcohols, when exposed to oxygen, are converted into CO_2 and H_2O as a result of a combustion reaction. Such reactions consist of several intermediate steps, which produce industrially valuable chemical species such as esters, ketones, carboxylic acids and aldehydes. These chemicals find uses in a wide range of applications in food, pharmaceutical, polymer and plating industries along with many others. As a result, there are considerable economical interests in the design of efficient, low-cost and environmentally low-impact synthetic routes of these products. Selective oxidation provides a way to interrupt the combustion reaction at the desired stage and extract the by-product of interest. The variety of these intermediate products and the particular mechanism is dictated by the environment and the catalyst used. Experimental studies have already indicated that the Au nanoparticles and Au surfaces pre-treated with atomic oxygen successfully catalyze selective oxidation. Current oxygen pretreatment

techniques are, however, difficult and costly.

The aim of this study is to design Au surfaces by means of doping the surface with Ni and Rh atoms in low concentrations to increase the performance of the surface for selective oxidation of ethanol. We utilize arguably the most successful theoretical method to ever have been used in surface science, namely Density Functional Theory (DFT), to understand the selective oxidation of ethanol. We present results concerning the dissociation of ethanol into subcomponents on these doped surfaces.

Keywords: Computational Physics, Density Functional Theory, Surface Physics, Catalysts

ÖZ

ALKOLLERİN ALTIN KATALİZÖRLER ÜZERINDE SEÇİCİ OKSİDASYON TEPKİME MEKANİZMALARININ YÜK YOĞUNLUĞU FONKSİYONELİ İLE İNCELENMESİ

Dernek, Ozan

Yüksek Lisans, Fizik Bölümü

Tez Yöneticisi : Doç. Dr. Hande Toffoli

Eylül 2016 , 49 sayfa

Alkollerin büyük bir çoğunluğu oksijene maruz bırakıldığında, yanma tepkimesi sonucunda CO_2 ve H_2O moleküllerine dönüşür. Bu gibi tepkimeler ester, keton, karboksil asit ve aldehid gibi endüstri için değerli kimyasalların oluştuğu ara basamaklardan meydana gelmektedir. Bu kimyasallar yiyecek, ilaç, polimer, kaplama ve benzerleri gibi geniş bir sektör yelpazesinde kullanılmaktadır. Bunun bir sonucu olarak, bu ürünlerin verimli, düşük maliyetli ve çevre dostu sentetik yöntemler ile üretilmesi ekonomik açıdan önem arz etmektedir. Seçici oksitlenme, yanma tepkimesine ara basamaklarda müdahale ederek istenilen ara ürüne ulaşım imkanı sağlamaktadır. Tepkime esnasında ortaya çıkan ara ürünlerin çeşitliliği ve oluşum mekanizmaları çevresel etkenler ve kullanılan katalizöre bağlıdır. Yapılan deneysel çalışmalarda atomik oksijen ile işlenmiş Au yüzeylerin ve Au nano parçacıkların seçici oksitlenmeyi katalize ettiği gözlemlenmiştir.

Ancak varolan yüzeyin oksijen ile işlenmesi yöntemleri teknik açıdan zor ve maliyetlidir.

Bu çalışmanın amacı Au yüzeyleri Ni ve Rh atomları ile düşük miktarlarda katkılayarak yüzeyin ethanol molekülünün seçici oksidasyon tepkimesini katalize etme performansını optimize etmektir. Ethanol molekülünün seçici oksidasyonunu anlamak adına, tartışmaya açık olarak, kullanılan en başarılı teorik yöntem olan Yük Yoğunluğu Fonksiyoneli (DFT) kullanıldı. Çalışmamızda ethanol molekülünün katkılı yüzeyler üzerinde altbileşenlerine ayrılması ile alakalı sonuçlar sunulmuştur.

Anahtar Kelimeler: Hesaplamalı Fizik, Yük Yoğunluğu Fonksiyoneli, Yüzey Fiziği, Kataliz

to my uncle, Sedat Dernek

ACKNOWLEDGMENTS

I am beholden to my supervisor Assoc. Prof. Dr. Hande Toffoli, who has been a wonderful tutor for me since my senior year, for her patiance and inspiring discussions throughout this study. The door to Prof. Toffoli' s office was always open when I needed her guidance.

I would like to express my sincere gratitute to Assoc. Prof. Dr. Emre Taşçı for his encouragement and motivational conversations that boosted my determination.

I also would like to express my gratitute to my colleague Duygu Gizem Şentürk for her support. She was always there for me when I was stressed out and never failed to cheer me up.

Last but not the least, I would like to thank all my friends and family for their endless support.

This work is supported by TÜBİTAK (The Science and Technological Research Council of Turkey)(Grant no:113F099)

TABLE OF CONTENTS

LIST OF TABLES

TABLES

LIST OF FIGURES

FIGURES

LIST OF ABBREVIATIONS

AE	All electron
DOS	Density of states
QE	Quantum Espresso
SCF	Self consistent field
PBE	Perdew Burke Ernzerhof
DFT	Density functional theory
LDA	Local density approximation
GGA	Generalized gradient approximation
PDOS	Partial Density of states
PWscf	Plane-wave self consistent field

CHAPTER 1

INTRODUCTION

Most of the fundamental industries are in need of chemical components for either developing new products, or maintaining a production rate fast enough to keep up with the increasing demand. According to the European Chemical Industry Council, in 2014, total sales of chemical products reached € 551 billion just by European companies, and the industry is growing annually [1]. These numerous chemicals are used in a broad range of products from polymers to food additives [2, 3]. Although there are chemicals that can be extracted from plants and animals, it is not possible to satisfy this need from nature itself. Hence, production of these chemicals by synthetic processes is mandatory. However, the process of producing such chemicals can be costly and harmful for the environment. According to the report published in 2013 by Intergovermental Panel on Climate Change, the global surface temperature will increase by 0.3 to 1.7 °C, in the best case scenario of the emission of greenhouse gasses, such as CO_2 [4].

Under these circumstances, the increase in the production rate of industrial chemicals necessitates green and low cost processes. Working on such technologies for this purpose, and developing new materials with better catalytic properties has been the main focus of a large body of recent studies. As a glimpse into these studies, one of the remarkable breakthroughs in materials chemistry is the periodic mesoporous organosilicas (PMOs), which show unique properties compared to other techniques in alkylation processes. [5–9]. Oxidation of elemental Hg^0 via catalytic means is another important study, aiming to reduce the air pollution caused by coal-fired power plants [10].

Among the chemicals used in various industries, alcohols hold an important place in terms of their variety, versatility and abundance. *Alcohol* is a general name given to an organic compound in which an (-OH) group is bonded to a fully saturated C atom. Alcohols can be divided into three categories, namely, primary, secondary and tertiary, based on the end groups attached to the C atom that binds the (-OH) group (see Fig. 1.1). Although the products of primary alcohols are more toxic than the secondary and tertiary alcohols, they are on focus of the industry, since they can be obtained by aerobic oxidation process and the byproduct of these reactions is generally water, which is a harmless molecule [11]. Moreover, especially in fuel production, the structural properties of such products make them more flammable, which makes alcohols more favorable [12]. In this thesis, we will concentrate on one of the smallest primary alcohols, i.e. ethanol.

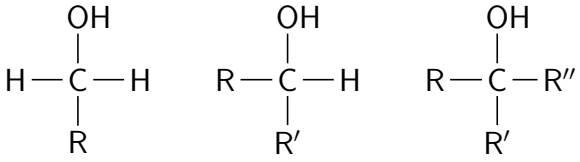

(a) (b) (c)

Figure 1.1: Primary (a), secondary (b) and tertiary (c) alcohols. R, R' and R'' represent possible end groups.

(a) (b)

Figure 1.2: Molecular structures of primary alcohols ethanol and methanol respectively.

An important industrial application involving alcohols is their selective oxidation in the presence of a catalyst. In this context, oxidation refers to the reduction of alcohols progressively to smaller species by means of losing their hydrogens to ambient O atoms or OH species and eventually to CO_2 and H_2O. An example is reproduced here in Fig. 1.3 from the work by Liu *et al.* [13], where the simplest alcohol, methanol (CH_3OH) is decomposed to CO_2 through a complicated reaction pathway.

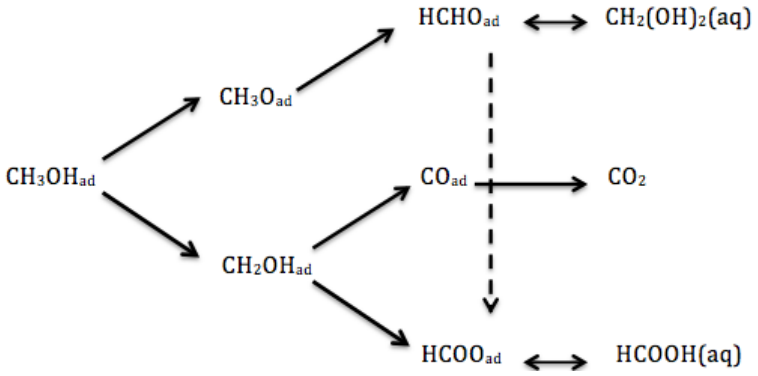

Figure 1.3: Reaction mechanism for the oxidation of methanol. Reproduced from Liu *et al.* [13].

During the multi-step oxidation reactions of primary alcohols, several intermediate products are produced that are of great value. Among these are esters, ketones, aldehydes and acids (Fig. 1.4) [14]. The particular reaction pathway and consequently the intermediates created depends sensitively on the environmental conditions. For instance, in the absence of ambient atomic or molecular oxygen, an ethanol to acetaldehyde reaction path has been proposed as follows [14]:

1. Adsorption of ethanol on the surface:

$$CH_3CH_2OH \longrightarrow CH_3CH_2OH^* \tag{1.1}$$

2. Dehydrogenation of adsorbed ethanol into ethoxy by means of the cleavage of the O−H bond :

$$CH_3CH_2OH^* \longrightarrow CH_3CH_2O^* + H^* \tag{1.2}$$

3. Further dehydrogenation of ethoxy into acetaldehyde by means of the ex-

traction of one of the β-H's:

$$CH_3CH_2O^* \longrightarrow CH_3CHO^* + H^* \tag{1.3}$$

In Eqs. 1.1 though 1.3, $*$ denotes a surface-adsorbed species. Dehydrogenation may occur through a slightly different reaction pathway in the presence of atomic oxygen on a pretreated catalyst surface [15]. H_2O is formed as a product at the end of this pathway.

$$\begin{aligned} &CH_3CH_2OH \longrightarrow CH_3CH_2O^* + H^* \\ &CH_3CH_2O^* + O^* \longrightarrow CH_3CHO^* + OH^* \\ &O^{*+}OH^* \longrightarrow H_2O \end{aligned} \tag{1.4}$$

The example in Eq. 1.4 terminates with the formation of H_2O, however, depending on the ambient conditions, other outcomes are also possible. The activation barriers associated with O-assisted oxidation tend to be smaller.

In the presence of ambient or surface oxygen, acetaldehyde may further be oxidized into acetic acid

$$CH_3CHO^* + O^* \longrightarrow CH_3COOH^* \tag{1.5}$$

For the formation of more complex intermediates such as larger ketones, esters, acids and aldehydes, coupling reactions are needed. These reactions involve various combinations of reactants and intermediates. A narrow list of examples from literature can be presented as follows:

1. Methoxy and formaldehyde to acetic acid [16]

$$CH_3O + CH_2O \longrightarrow CH_3COOH \tag{1.6}$$

2. Acetaldehyde and ethoxy to ethyl acetate [17]

$$CH_3CHO + CH_3CH_2O \longrightarrow CH_3COOCH_2CH_3 + H \tag{1.7}$$

3. Self-coupling of hydroxyethyl to ethanol and ethoxy [18]

$$CH_3CHOH + CH_3CHOH \longrightarrow CH_3CH_2OH + CH_3CHO \tag{1.8}$$

The process of oxidation of alcohols is usually facilitated by the use of a catalyst. Some of the catalysts that have been used for this purpose are Pd(II) [19], Pt/Al_2O_3 [20], Co_3O_4 [21]. Due to the high volume demand of products created in the alcohol oxidation process, developing new catalytic materials to reduce the cost and damage to the environment of these products is crucial. After the study of Haruta *et al.* [22], Au-based catalysts gathered remarkable interest in the catalytic society. Following this inspiring study, various techniques and bimetallic systems are developed to increase the catalytic properties of Au.

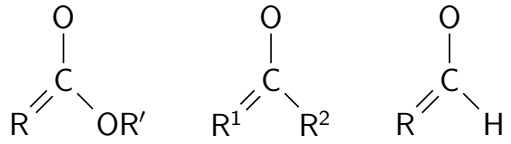

(a) (b) (c)

Figure 1.4: Some of the intermediates; esters, ketones and aldehyde which may occur during an oxidation process.

Until recently, Au was known to be a chemically inert element. The pioneering work by Haruta *et al.* [22], proved instead that Au-based catalysts can improve the oxidation of CO in the temperatures well below the room temperature. They reported that combining Au with α-Fe_2O_3, Co_3O_4 or NiO shows great catalytic activity and stability in the oxidation process of CO. Since then, Au-based nanoparticles and surfaces have been extensively used to promote oxidation, dehydrogenation, dissociation reactions of organic compounds, as well as water-gas shift reactions [23–31].

In this thesis, we have focused on Au based surface catalysts instead as a means of modeling both bulk and nano-scale systems. In many studies, activation of Au surfaces have been achieved by oxidation of the surface, by using various techniques, i.e. ozone decomposition, oxygen sputtering and so on [32]. Since this process is costly and technically challenging, new strategies to enhance the surface activation of Au based catalysts have been developed. Among these methods, surface alloying is one of the most successful strategies [33–35]. Substituting transition metals on (111) Au surfaces has been proven to be an effective method to enhance the catalytic activity of the surface. The surface

activity of transition metals is largely controlled by their d orbitals. Introducing transition metals to (111) Au surfaces can modify the surface activity in favor of adsorption of chemical compounds. The mechanics behind this technique will be explained in the following chapter.

The literature on this topic has a large variety of studies. In the study of Liu et. al [36], it is reported that methanol oxidation over O-covered (111) Au surface can yield to formation of methyl formate or formate, depending on the oxygen coverage. Another study about the adsorption and dissociation of methanol on (111) Au surface reports that methanol oxidation can yield to formation of formaldehyde with low energy cost.

In the study of Qingsen *et al.*, it is reported that selective oxidation of ethanol over Au surfaces by activating the O-H bond is favorable in the presence of surface oxygen adatom [15]. It is also stated that β- H elimination of obtained ethoxy is more energy costly than obtaining the ethoxy itself, which means further reactions are not favorable because of the high energy barriers.

In a Au based heterostructral study, it is reported that Au-Pd alloy of Au_3Pd mixture weakens the butane adsorption on the surface compared to pure (111) Pd surface, which leads to an enhancement of the selectivity of the surface [11]. Moreover, in a study related to the purification of the surface, it is stated that Au-Pd alloy enhance methanol oxidation reaction in which Pd atoms serve as activation center and Au atoms assist to the elimination of the product from surface [37].

Although Au has been proven to be a successful catalyst, it is obvious that its catalytic properties can be enhanced by powerful alloying and tailoring methods for better quality.

CHAPTER 2

DENSITY FUNCTIONAL THEORY

In many-particle interacting systems, the Schrödinger equation is intractable. Fortunately, density functional theory (DFT) proposes an elegant calculation method to overcome this problem, by utilizing the idea of "*electron density*" and the fundamentals of quantum mechanics. The DFT has a great impact in materials modeling in a very large scale from catalysis to biomaterials [38]. In the work of Olson *et al.*, it is stated that DFT is being used for the calculations of strength increase of steel in Ford Motor Company [39]. From a completely different subject, Sugihara *et al.* utilized DFT to investigate the properties of retinal chromophore in rhodopsins [40]. The fundamentals of DFT is dealing with the objects that construct the life. Hence, it is a crucial theory for any scientist, especially for physicists who are interested in molecular and nano scales.

2.1 The Many-Body Hamiltonian

In a quantum mechanical many-particle system, all relevant information can be acquired from the wave functions. The wave functions, in turn, can be obtained by solving the Schrödinger equation, which yields the ground and excited state energies of the system as eigenvalues:

$$\hat{H}\psi(\vec{r_1},...,\vec{r_N};\vec{R_1},...,\vec{R_M}) = E\psi(\vec{r_1},...,\vec{r_N};\vec{R_1},...,\vec{R_M}), \tag{2.1}$$

where $\{\vec{r_i}\}$ and $\{\vec{R_I}\}$ are the electronic and nuclear positions. The many-particle Hamiltonian in Eq. 2.1 is

$$\hat{H} = \hat{T}_n + \hat{T}_e + \hat{V}_{nn} + \hat{V}_{ne} + \hat{V}_{ee}. \tag{2.2}$$

In Eq. 2.2 the terms, represent the kinetic energy of nuclei, the kinetic energy of electrons, Coulombic potential energy of nuclei-nuclei interaction, Coulombic potential energy of nuclei-electron interaction and Coulombic potential energy of electron-electron interaction, respectively. In a more explicit representation,

$$\hat{H} = -\frac{1}{2}\sum_{I=1}^{N_n}\frac{1}{M_I}\nabla^2_{\vec{R}_I} - \frac{1}{2}\sum_{i=1}^{N_e}\nabla^2_{\vec{r}_i} + \frac{1}{2}\sum_{J\neq I}^{N_n}\frac{Z_I Z_J}{|\vec{R}_I - \vec{R}_J|} - \sum_{I=1}^{N_n}\sum_{i=1}^{N_e}\frac{Z_I}{|\vec{r}_i - \vec{R}_I|} + \frac{1}{2}\sum_{i}^{N_e}\sum_{j\neq i}^{N_e}\frac{1}{|\vec{r}_i - \vec{r}_j|} \tag{2.3}$$

where atomic units ($\hbar = m_e = \frac{1}{4\pi\epsilon_0} = 1$) have been utilized. In Eq. 2.3, Z_I is the nucleus with the mass M_I located at $\vec{R}_I$, Z_J is the nucleus that is located at R_J; while r_i and r_j are the positions of the electrons. The factor of $\frac{1}{2}$ in the third and fifth terms is necessary to avoid double counting.

Although the Hamiltonian in Eq. 2.3 treats both the electrons and the nuclei quantum mechanically, in practice, the nuclei are about 1000 times heavier than electrons. Therefore they can, in fact, be treated classically within the Born-Oppenheimer approximation. In a typical DFT calculation they are treated as *fixed* particles. In the light of this information, the potential term of nuclei-nuclei interaction V_{nn} can be considered a constant while the electrons follow the motion of the nuclei adiabatically, i.e. without delay. With these assumptions, the wave function can be separated into nuclear and electronic parts as:

$$\psi(\vec{r}, \vec{R}) = \sum_i \phi_n(\vec{R})\psi_{el}(\vec{r}, \vec{R}) \tag{2.4}$$

where the term $\phi_n(\vec{R})$ represents the nuclear wave function. This simplification allows us to separate the electronic and the nuclear parts of the Hamiltonian. Here, we concentrate on the electronic part, which is given as

$$\begin{aligned}\hat{H} &\equiv \hat{T}_e + \hat{V}_{ne} + \hat{V}_{ee} \\ &= -\frac{1}{2}\sum_{i=1}^{N_e}\nabla^2_{\vec{r}_i} - \sum_{I=1}^{N_n}\sum_{i=1}^{N_e}\frac{Z_I}{|\vec{ri} - \vec{R}_I|} + \frac{1}{2}\sum_{i}^{N_e}\sum_{j\neq i}^{N_e}\frac{1}{|\vec{r}_i - \vec{r}_j|}\end{aligned} \tag{2.5}$$

The electronic Schrödinger equation is then

$$\hat{H}_{el}\psi_{el} = E_{el}(\vec{R})\psi_{el}(\vec{r}, \vec{R}), \tag{2.6}$$

where the nuclear positions appear only as a set of parameters. In this sense, each nuclear arrangement corresponds to a new set of eigenvalues and eigenfunctions.

2.2 The Electron Density

The exact or even a very accurate numerical solution of Eq. 2.6 is impossible to achieve even for the smallest systems. As mentioned previously, DFT offers an alternative to the direct solution in terms of the wavefunction. The focus of the problem becomes, instead, the electronic density, which can be defined via the usual one-particle electron density operator,

$$\hat{\rho}(\vec{r}) = \sum_{i=1}^{N} \delta(\vec{r} - \vec{r}_i). \tag{2.7}$$

This operator is related to the probably of finding an electron at an arbitrary point, $\vec{r}$, in three-dimensional space. Substituting Eq. 2.7 into the many-body wave function yields

$$\begin{aligned} \rho(\vec{r}) = & \langle \psi(\vec{r}_1, ..., \vec{r}_N) | \, \hat{\rho}(\vec{r}) \, | \psi(\vec{r}_1, ..., \vec{r}_N) \rangle \\ = & \sum_{i=1}^{N} \int \delta(\vec{r} - \vec{r}_i) |\psi(\vec{r}_1, \vec{r}_2, ..., \vec{r}_N)|^2 d\vec{r}_1 d\vec{r}_2 ... d\vec{r}_N. \end{aligned} \tag{2.8}$$

Performing the δ-function integrals over each variable and affecting a subsequent change of variables yields the electronic density,

$$\rho(\vec{r}) = N \int |\psi(\vec{r}, \vec{r}_2, ..., \vec{r}_N)|^2 d\vec{r}_2 d\vec{r}_3 ... d\vec{r}_N. \tag{2.9}$$

The electronic density is then a simple integral over all but one of the electronic variables of the norm square of the wavefunction. Integration over all space gives the total number of electrons present in the system, which defines the normalization of the density

$$\int \rho(\vec{r}) d\vec{r} = N. \tag{2.10}$$

2.2.1 Energy Representation in Terms of Electron Density

Utilizing the density operator, each term in the electronic Hamiltonian can be represented in terms of electron density. The expectation value of $\hat{H}_{el}$ is

$$\langle\psi(\vec{r}_1,...,\vec{r}_N)|\,\hat{H}_{el}\,|\psi(\vec{r}_1,...,\vec{r}_N)\rangle = \langle\psi(\vec{r}_1,...,\vec{r}_N)|\,\hat{T}_e + \hat{V}_{ee} + \vec{V}_{ne}\,|\psi(\vec{r}_{1,...,\vec{r}_N})\rangle\,. \tag{2.11}$$

The Eq. 2.11 can be handled term by term. Beginning with the kinetic energy term, expectation value is:

$$T_e = \langle\psi(\vec{r}_1,...,\vec{r}_N)|\,\hat{T}_e\,|\psi(\vec{r}_1,...,\vec{r}_N)\rangle = -\frac{1}{2}\sum_{i=1}^{N_e}\int \psi^*(\vec{r}_1,...,\vec{r}_N)\nabla^2_{\vec{r}_i}\psi(\vec{r}_1,...,\vec{r}_N). \tag{2.12}$$

Here, one should be careful about the derivative term in the kinetic energy. Due to this term, for an interaction system, it is not possible to define the kinetic energy operator in terms of density. Therefore, an assumption of non-interaction system should be utilized. This assumption is proposed by Kohn and Sham [41], stating that an identical density to the true system of non-interacting particles should be considered:

$$\rho(\vec{r}) = \sum_{n}^{N_e}|\phi_e(\vec{r})|^2. \tag{2.13}$$

By defining the kinetic energy in terms of Eq. 2.13, one obtains:

$$T_e = -\frac{1}{2}\sum_{n}^{N_e}\int \phi_e^*(\vec{r})\nabla^2\phi_e(\vec{r})d\vec{r} + \Delta T_e \tag{2.14}$$

where ΔT_e is added as a correction to the non-interacting system to establish the convenience between the auxiliary and true system.

The second term, V_{ne}, is rather easy since there is no derivative in the energy operator:

$$\begin{aligned} V_{ne} &= \langle\psi(\vec{r}_1,\cdots,\vec{r}_N)|\,\hat{V}_{ne}\,|\psi(\vec{r}_1,\cdots,\vec{r}_N)\rangle \\ &= -\sum_{i=1}^{N_e}\sum_{I=1}^{N_I}\int \frac{Z_I}{|\vec{r_i}-\vec{R}_I|}|\psi(\vec{r}_1,\cdots,\vec{R}_I)|^2 d\vec{r}_1,\cdots,d\vec{r}_N. \end{aligned} \tag{2.15}$$

Writing the sum over the electron explicitly and seperating the Coulombic and

wave function terms, one gets:

$$V_{ne} = -\sum_{I=1}^{N_I}\left[\int \frac{Z_I}{|\vec{r}_1 - \vec{R}_I|}d\vec{r}_1 \underbrace{\int |\psi(\vec{r}_1,\cdots,\vec{r}_N)|^2 d\vec{r}_2 d\vec{r}_3\cdots d\vec{r}_N}_{\rho(\vec{r}_1)} \right.$$
$$\left. + \int \frac{Z_I}{|\vec{r}_2 - \vec{R}_I|}d\vec{r}_2 \underbrace{\int |\psi(\vec{r}_1,\cdots,\vec{r}_N)|^2 d\vec{r}_1 d\vec{r}_3\cdots d\vec{r}_N}_{\rho(\vec{r}_2)} + \cdots\right] \quad (2.16)$$

since the integral over the norm square of the wave function in each term is equal to the density. Using this identity to rearrange Eq. 2.16 gives:

$$V_{ne} = -\frac{1}{N_e}\sum_{I=1}^{N_I}\left[\int \frac{Z_I}{|\vec{r}_1 - \vec{R}_I|}d\vec{r}_1\rho(\vec{r}_1) + \int \frac{Z_I}{|\vec{r}_1 - \vec{R}_I|}d\vec{r}_2\rho(\vec{r}_2) + ...\right]. \quad (2.17)$$

If the index of each density argument in the integrals is replaced by a dummy index, all the integral terms become same. Since there are N_e number of terms in the equation, it becomes:

$$V_{ne} = -\sum_{I=1}^{N_I}\int \rho(\vec{r})\frac{Z_I}{|\vec{r} - \vec{R}_I|}d\vec{r} = \int \rho(\vec{r})\hat{V}_{ne}d\vec{r}. \quad (2.18)$$

The expectation value of the final term, the Coulomb potential due to the electron-electron interaction V_{ee} is:

$$V_{ee} = \langle\psi(\vec{r}_1,...,\vec{r}_N)|\,\hat{V}_{ee}\,|\psi(\vec{r}_1,...,\vec{r}_N)\rangle$$
$$= \frac{1}{2}\sum_{i}^{N_e}\sum_{j\neq i}^{N_e}\int \frac{1}{|\vec{r}_i - \vec{r}_j|}|\psi(\vec{r}_1,...,\vec{r}_N)|^2 d\vec{r}_1...d\vec{r}_N. \quad (2.19)$$

Writing the sums explicitly and separating the integration over the norm square of wave function gives:

$$V_{ee} = \frac{1}{2}\left[\iint \frac{1}{|\vec{r}_1 - \vec{r}_2|}d\vec{r}_1 d\vec{r}_2 \int |\psi(\vec{r}_1,\cdots,\vec{r}_N)|^2 d\vec{r}_3 d\vec{r}_4...d\vec{r}_N \right.$$
$$\left. + \iint \frac{1}{|\vec{r}_1 - \vec{r}_3|}d\vec{r}_1 d\vec{r}_3 \int |\psi(\vec{r}_1,\cdots,\vec{r}_N)|^2 d\vec{r}_2 d\vec{r}_4\cdots d\vec{r}_N\right]. \quad (2.20)$$

However, this term cannot be described as the term V_{ne} since it depends on the relative position of two electrons. Therefore, it would be more appropriate to define a two-particle density operator, $\hat{\rho}(\vec{r},\vec{r'})$:

$$\hat{\rho}(\vec{r},\vec{r'}) = \sum_{i}^{N_e}\sum_{j}^{N_e}\delta(\vec{r} - \vec{r}_i)\delta(\vec{r'} - \vec{r}_j) \quad (2.21)$$

with the expectation value:

$$\rho(\vec{r},\vec{r'}) = \frac{N_e(N_e-1)}{2}\int |\psi(\vec{r},\vec{r'},\vec{r}_3,\vec{r}_4,...,\vec{r}_N|^2 d\vec{r}_3\vec{r}_4...d\vec{r}_N. \tag{2.22}$$

Rewriting the Eq. 2.19 in terms of $\rho(\vec{r},\vec{r'})$ gives:

$$V_{ee} = \frac{1}{2}\frac{2}{N_e(N_e-1)}\left[\iint \frac{\rho(\vec{r}_1,\vec{r}_2)}{|\vec{r}_1-\vec{r}_2|}d\vec{r}_1 d\vec{r}_2 + \iint \frac{\rho(\vec{r}_1,\vec{r}_3)}{|\vec{r}_1-\vec{r}_3|}d\vec{r}_1 d\vec{r}_3 + ...\right]. \tag{2.23}$$

Rearranging the index of density arguments in each integral will result as:

$$V_{ee} = \frac{1}{2}\iint \frac{\rho(\vec{r},\vec{r'})}{|\vec{r}-\vec{r'}|}d\vec{r}d\vec{r'} \tag{2.24}$$

where $\rho(\vec{r},\vec{r'})$ is the two-electron density, which is related to the probability of finding an electron pair at the positions $\vec{r}$ and $\vec{r'}$. Unlike the other terms, this term cannot be reduced any further to an expression in terms of the one-particle density. Instead, we break it down into two parts: a classical electrostatic interaction term and a correction that holds the quantum mechanical corrections

$$\rho(\vec{r},\vec{r'}) = \rho(\vec{r})\rho(\vec{r'}) + \Delta\rho(\vec{r},\vec{r'}). \tag{2.25}$$

Using this definition, finally V_{ee} becomes:

$$V_{ee} = \frac{1}{2}\iint \frac{\rho(\vec{r})\rho(\vec{r'})}{|\vec{r}-\vec{r'}|}d\vec{r}d\vec{r'} + \Delta V_{ee}. \tag{2.26}$$

Now that all the expectation values have been found in terms of density except the exhange correlation energy E_{xc}, total ground state electronic energy is:

$$\begin{aligned} E_{el} = T_e + V_{ne} + V_{ee} = &-\frac{1}{2}\sum_n^{N_e}\int \phi_e^*(\vec{r})\nabla^2\phi_e(\vec{r})d\vec{r} + \int \rho(\vec{r})\hat{V}_{ne}d\vec{r} \\ &+ \frac{1}{2}\iint \frac{\rho(\vec{r})\rho(\vec{r'})}{|\vec{r}-\vec{r'}|}d\vec{r}d\vec{r'} + \underbrace{\Delta T_e + \Delta V_{ee}}_{\mathrm{E}_{xc}} \end{aligned} \tag{2.27}$$

where the very last term, exchange-correlation energy E_{xc} is the correction term, which avoids the difference between the *non-interacting* system and the real system.

2.3 The Hohenberg-Kohn Theorems and Kohn-Sham Equations

The final expression for energy in Eq. 2.27 is so far exact. Thus, in theory, if the minimum of E_{el} obtained by means of a functional derivative with respect to

all of the Kohn-Sham orbitals, ϕ_i, will yield the ground state energy. However, before this can be done the existence and the uniqueness of this minimum must be ensured. This was done by two simple yet elegant theorems in 1964 by Hohenberg and Kohn [42].

The first theorem states that the density is uniquely determined by the external potential $V_{ext}(\vec{r})$. For the proof of this theorem, two different potentials V_1^{ext} and V_2^{ext} that lead to same ground state density $n(\vec{r})$ should be considered. However, these two potentials would have different wave functions, since they belong to different Hamiltonians $\hat{H}_1$ and $\hat{H}_2$. Calculating the expectation value of these two Hamiltonians, one obtains the inequality:

$$E_1 = \langle \psi_1 | \hat{H}_1 | \psi_1 \rangle < \langle \psi_2 | \hat{H}_2 | \psi_2 \rangle . \tag{2.28}$$

Eq. 2.28 is an obvious result according to the variational principle, unless the ground state is degenerate. With the above assumption that both potentials V_1^{ext} and V_2^{ext} give rise to the same ground state density, one can connect the two Hamiltonians by:

$$\langle \psi_2 | \hat{H}_1 | \psi_2 \rangle = \langle \psi_2 | \hat{H}_2 | \psi_2 \rangle + \int d\vec{r} \left[V_1^{ext}(\vec{r}) - V_2^{ext}(\vec{r}) \right] n_o(\vec{r}). \tag{2.29}$$

Similarly:

$$\langle \psi_1 | \hat{H}_2 | \psi_1 \rangle = \langle \psi_1 | \hat{H}_1 | \psi_1 \rangle + \int d\vec{r} \left[V_2^{ext}(\vec{r}) - V_1^{ext}(\vec{r}) \right] n_o(\vec{r}). \tag{2.30}$$

Summing Eq. 2.29 and Eq. 2.30 leads to an obvious contradiction:

$$E_1 + E_2 < E_2 + E_1. \tag{2.31}$$

Therefore it is proven that the ground state density is uniquely obtained by the ground state potential.

Although the first theorem is essential, a practical implementation of this idea is needed, which is provided in the second theorem by using variational principle. In their second theorem, Hohenberg and Kohn stated that the density that minimizes the energy is ground state density, and no other density different from the ground state density can yield a smaller energy than the ground state energy:

$$E[\rho] > E_0[\rho_0] = E_0 \tag{2.32}$$

where E_0 is the ground state energy, ρ_0 is the ground state density and ρ is some random density. After stating the second theorem, a mathematical expression of the first theorem is available:

$$\langle\psi|\,\hat{H}\,|\psi\rangle = T_e[\rho] + V_{ee}[\rho] + \int \rho(\vec{r})V_{ext}d\vec{r} = E[\rho] \geqslant E_0[\rho] = \langle\psi_0|\,\hat{H}\,|\psi_0\rangle\,. \quad (2.33)$$

The Hohenberg-Kohn theorems ensure that total energy of a system in its ground state is a functional of the electron density by achieving one-to-oneness and uniqueness. Reproducing Eq. 2.27 here:

$$\begin{aligned} E_{el}[\rho(\vec{r})] &= T_e[\rho(\vec{r})] + V_{ne}[\rho(\vec{r})] + V_{ee}[\rho(\vec{r})] \\ &= \underbrace{-\frac{1}{2}\sum_n^{N_e}\int \phi_e^*(\vec{r})\nabla^2\phi_e(\vec{r})d\vec{r}}_{\text{Kinetic Energy}} + \underbrace{\int \rho(\vec{r})\hat{V}_{ne}d\vec{r}}_{\text{External Potential}} \\ &+ \underbrace{\frac{1}{2}\iint \frac{\rho(\vec{r})\rho(\vec{r'})}{|\vec{r}-\vec{r'}|}d\vec{r}d\vec{r'}}_{\text{Hartree Energy}} + E_{xc}[\rho\vec{r}]. \end{aligned} \quad (2.34)$$

Here E_{xc} represents the electron exchange and correlation. It is also a result of the theorems that minimization of this energy yields to the ground state wave function. The minimization of the energy is done by taking the functional derivative of Eq. 2.34 with respect to non-interacting, orthonormal orbital set, namely Kohn-Sham orbitals, which gives:

$$\frac{\delta E}{\delta\phi_i^*(\vec{r})} = \frac{\delta T_e}{\delta\phi_i^*(\vec{r})} + \left[\frac{\delta E_{ext}}{\delta n(\vec{r})} + \frac{\delta E_{Hartree}}{\delta n(\vec{r})} + \frac{\delta E_{xc}}{\delta n(\vec{r})}\right]\frac{\delta n(\vec{r})}{\delta\phi_i^*(\vec{r})} = \varepsilon_i\phi_i(\vec{r}) \quad (2.35)$$

Here ε_i originate as Lagrange multipliers that keep $\{\phi_i\}$ orthogonal during minimization. With the energy expression in Eq. 2.34, Eq. 2.35 yields,

$$-\frac{1}{2}\nabla^2\phi_i^2(\vec{r}) + \left[V_{ext}(\vec{r}) + \int d\vec{r'}\frac{n(\vec{r'})}{|\vec{r}-\vec{r'}|} + V_{xc}\right]\phi_i(\vec{r}) = \varepsilon_i\phi_i(\vec{r}), \quad (2.36)$$

or more concisely,

$$\left[\hat{T} + V_{eff}\right]\phi_i(\vec{r}) = \varepsilon_i\phi_i(\vec{r}) \quad (2.37)$$

where V_{eff} includes the influence of all other occupied orbitals on the reference orbital $\phi_i(\vec{r})$ in a mean-fiel-like manner.

Finally, the Schrödinger equation is replaced by a solvable expression in terms of single particle orbitals. The term V_{eff} depends on the density, while it is

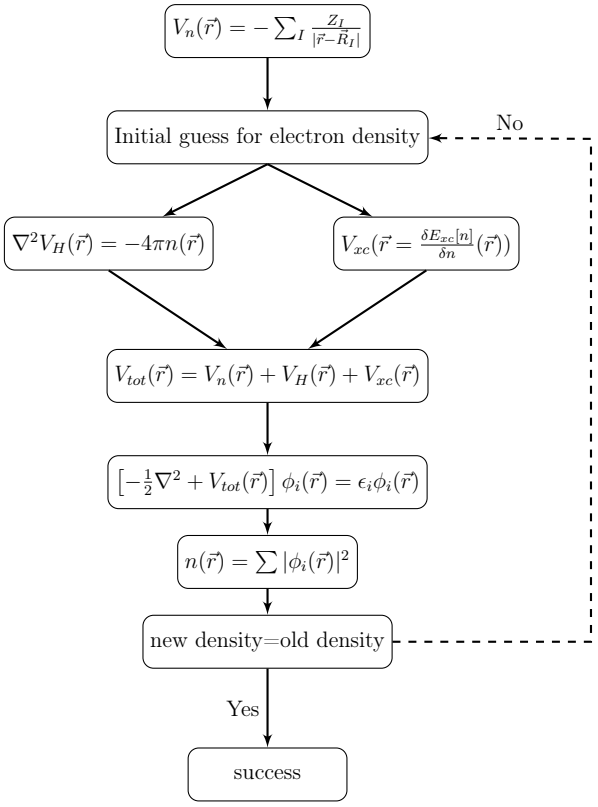

Figure 2.1: Flow chart presentation of self consistency calculations.

supposed to give the resultant energy after the solution of Eq. 2.37. The nonlinearity of the Kohn-Sham equations can be handled by self-consistent calculation. Moreover, the exchange correlation energy is waiting to be determined.

2.4 Practical Concerns

Although the theoretical foundations of DFT are straightforward, several practical challenges arise within an actual calculation. In this section, we will address these challenges and briefly summarize the solutions that have been developed over the years.

2.4.1 Exhange-Correlation Functionals

The success of the DFT calculations depends on the accuracy of the exchange correlation energy estimate to the real value. The below equation is the general

representation of exchange-correlation energy:

$$E_{xc}[\rho(\vec{r})] = \int e_{xc}(\vec{r}; [\rho(\vec{r'})])\rho(\vec{r})dr \tag{2.38}$$

where the term e_{xc} is the exchange-correlation energy at point r. Basically the term represents the effect of an electron on the density distribution of the system. The simplest approximation to Eq. 2.38 is the *so-called local density approximation* (LDA), in which the exchange correlation of a homogeneous electron gas $\epsilon_{xc}^{hom}(\mathrm{n}(\vec{r}))$ is utilized. Assuming that the density fluctuations in the real system are mild, the exchange-correlation energy at point $\vec{r}$ in the true system is written as

$$E_{xc}^{LDA} = \int d\vec{r}\rho(\vec{r})\epsilon_{xc}^{hom}(\rho(\vec{r})). \tag{2.39}$$

The contribution of the exchange-correlation term to the effective potential in Eq. 2.37 is given within LDA as

$$\hat{V}_{xc}^{LDA}(\vec{r}) = \frac{\delta E_{xc}^{LDA}[\rho]}{\delta\rho(\vec{r})} = E_{xc}(\rho(\vec{r})) + \rho(\vec{r})\frac{\partial E_{xc}}{\partial\rho}. \tag{2.40}$$

The exchange-correlation energy may further be developed by means of the inclusion of derivatives of the density. This approach accommodates inhomogeneities in the density more accurately, and is therefore more commonly used in systems where there are sharp changes in the density, such as surfaces. A popular formulation including derivatives is the *generalized gradient approximation*, written as [43]

$$E_{xc}^{GGA} = \int \rho(\vec{r})E_{xc}[\rho(\vec{r}), \nabla\rho(\vec{r})]d\vec{r}. \tag{2.41}$$

2.4.2 Plane-Wave Expansions

The Kohn-Sham equations fulfill the need to simplify the otherwise intractable many-body description. However, their solutions in real space is extremely hard. Therefore, considering the periodic boundary conditions, naturally occuring in crystals, it is more convenient to handle the problem in a plane wave basis set, by expanding the Kohn-Sham orbitals as follows,

$$\phi_i(\vec{r}) = \frac{1}{\sqrt{\Omega}}\sum c_{i,\vec{q}}\ \exp(i\vec{q}\cdot\vec{r}) \equiv \sum_{\vec{q}} c_{i,\vec{q}}\,|\vec{q}\rangle\,, \tag{2.42}$$

where $c_{i,\vec{q}}$ is the expansion coefficient and Ω is the volume of the crystal. It is possible to rewrite the Kohn-Sham equations in matrix form in a few steps by introducing this definition into Eq. 2.42, multiplying it from the left by $\langle\vec{q'}|$ and integrating in real space:

$$\sum_{\vec{q}} c_{i,\vec{q}} \langle\vec{q'}| \hat{H}_{KS} |\vec{q}\rangle = \epsilon_i \sum_{\vec{q}} c_{i,\vec{q}} \langle\vec{q'}|\vec{q}\rangle = \epsilon_i c_{i,\vec{q}}. \tag{2.43}$$

In matrix notation, this can be written as

$$\tilde{H}C = \epsilon C \tag{2.44}$$

where $\tilde{H}$ is the matrix representation of the Hamiltonian and C is the vector of coefficients. In this representation, the kinetic term is rather simple:

$$\langle\vec{q'}| -\frac{1}{2}\nabla^2 |\vec{q}\rangle = \frac{1}{2}|\vec{q}|^2 \delta_{\vec{q}\vec{q}'}. \tag{2.45}$$

The effective potential energy term V_{eff} can be expressed as a Fourier transform, where the only nonzero Fourier components are those that correspond to reciprocal space vectors:

$$\hat{V}_{eff}(\vec{r}) = \sum_m \hat{V}_{eff}(\vec{G}_m) \exp\Big(i\vec{G}_m \cdot \vec{r}\Big). \tag{2.46}$$

In Eq. 2.46, $\{\vec{G}_m\}$ are the wavevectors in the reciprocal space. Here, the Fourier component $V_{eff}(\vec{G})$ is defined as

$$\hat{V}_{eff}(\vec{G}) = \frac{1}{\Omega_{cell}} \int_{\Omega_{cell}} \hat{V}_{eff}(\vec{r}) \exp\Big(-i\vec{G} \cdot \vec{r}\Big) d\vec{r}. \tag{2.47}$$

Inserting the Eq. 2.47 into Eq. 2.43, we have

$$\begin{aligned} \langle\vec{q'}| \hat{V}_{eff} |\vec{q}\rangle &= \sum_m \left\langle \vec{q'} \right| \hat{V}_{eff}(\vec{G}_m) \left|\vec{q}\right\rangle \exp\Big(i\vec{G}_m \cdot \vec{r}\Big) \equiv \sum \left\langle \vec{q'} \right| \hat{V}_{eff}(\vec{G}_m) \left|\vec{q} + \vec{G}_m\right\rangle \\ &= \sum_m V_{eff}(\vec{G}_m) \left\langle \vec{q'} \middle| \vec{q} + \vec{G_m} \right\rangle = \sum_m V_{eff}(\vec{G}_m) \delta_{\vec{q'}-\vec{q},\vec{G}_m}. \end{aligned} \tag{2.48}$$

Eq. 2.48 implies that the terms that contribute to the effective potential are the ones with wavevectors that differ by a reciprocal lattice vector. By making the definitions $\vec{q} = \vec{k} + \vec{G}_m$ and $\vec{q'} = \vec{k} + \vec{G'}_m$, the matrix representation takes form:

$$\sum_m \left\langle \vec{k} + \vec{G'}_{m'} \right| \hat{H}_{eff} \left| \vec{k} + \vec{G}_m \right\rangle c_{i,m} = \epsilon_i c_{i,m'} \tag{2.49}$$

for a given $\vec{k}$, where $\vec{q}$ and $\vec{q'}$ differ by a reciprocal lattice vector. Eq. 2.49 can be shortened to

$$\sum_{m} \hat{H}_{m,m'}(\vec{k}) c_{i,m}(\vec{k}) = \epsilon_i(\vec{k}) c_{i,m'}(\vec{k}). \tag{2.50}$$

In the calculations, plane-waves under a certain energy limit are omitted to reduce the computational cost, i.e.

$$\frac{1}{2}|\vec{G} + \vec{q}|^2 < E_{cut}. \tag{2.51}$$

In general, a suitable value of E_{cut} is determined by means of a convergence test using some figure of merit such as total energy.

2.5 The Concept of Pseudopotentials

While the core electrons are strictly localized around the nuclei, the valence electrons are responsible for the electronic and bonding characteristics of materials. The core electrons, while mostly inert, screen the nuclear potential and affect the behavior of the valence electrons indirectly. Therefore, an effective potential can be deviced that takes into account the Coulomb potential of the nuclei and the screening effect of the core electrons. Once this is done, the core electrons may be completely removed from the calculation and replaced by the frozen effective potential, namely the *pseudopotential*. A pseudopotential, generated for an isolated atom and then ported to the actual calculation, has the effect of reducing the total number of electrons while at the same time reducing the energy cutoff by eliminating oscillatory behavior of the valence electrons around the nuclei.

A successfully generated pseudopotential should hold four distinct properties:

1. The energy spectrum of the true (referred often as *all-electron* or AE) Coulombic potential and the pseudopotential must be identical.

$$\hat{H} \left|\phi^{(R)}\right\rangle = \epsilon_i \left|\phi_i^{(R)}\right\rangle \left(\hat{H} + V_{PS}\right) \left|\phi_i^{(PS)}\right\rangle = \epsilon_i \left|\phi_i^{PS}\right\rangle. \tag{2.52}$$

2. The real wave functions and pseudowavefunctions must be same outside

of the core region $r > r_c$,

$$\phi_i^{(R)}(r) = \phi_i^{(PS)}(r), \tag{2.53}$$

for a suitably chosen r_c.

3. The norm squares of both wave functions must be equal inside the core region $r < r_c$:

$$\int_0^{r_c} |\phi^R(r)|^2 r^2 dr = \int_0^{r_c} |\phi^{PS}(r)|^2 r^2 dr \tag{2.54}$$

4. The logarithmic derivatives and the energy derivative of the logarithmic derivative agree for all $r < r_c$:

$$\left[(r\phi^R(r))^2 \frac{d}{dE}\frac{d}{dr}\ln\phi^R(r)\right]_r = \left[(r\phi^{PS}(r))^2 \frac{d}{dE}\frac{d}{dr}\ln\phi^{PS}(r)\right]_r \tag{2.55}$$

In this work, ultrasoft pseudopotentials have been used, which requires noticeably lower plane wave basis cutoff with respect to the standard augmented plane wave methods, while performing equivalent accuracy with rapid convergence [44].

2.6 Implementation of DFT in the Quantum Espresso

There are several computational packages that implement DFT used in materials modeling. Quantum-Espresso (QE) is an open-source package based on plane-wave self consistent field (PWscf) approach [45]. After setting the necessary parameters and choice of an appropriate pseudopotential by user, QE performs self-consistency calculations to solve Kohn-Sham equations. After each iteration, the resulting density is compared with the old one. This iterative process continues untill there is no difference between last two successive calculations. This means a ground state density is achieved.

2.6.1 Structure Relaxation

A relaxation calculation is a set of successive SCF calculations which performs a geometric optimization to minimize the net force on atoms in the system:

$$F_i = -\frac{\partial E}{\partial R_i} \tag{2.56}$$

where R_i is the position of the nuclei. This calculation is done by utilizing Hellmann-Feynman theorem [46], which states that derivative of the energy with respect to a parameter can be found by calculating the expectation value of the derivative of the Hamiltonian operator with respect to that same parameter:

$$F_i = -\frac{\partial}{\partial R_i} \langle\psi| \hat{H} |\psi\rangle = -\langle\psi| \frac{\partial \hat{H}}{\partial R_i} |\psi\rangle . \tag{2.57}$$

The forces, defined above are only valid at the electronic ground state. A geometry optimization procedure is conducted iteratively in the following way. For a given initial set of nuclear coordinates, the calculations of the electronic ground state is performed, followed by the calculation of the forces according to Eq. 2.57. The nuclei are then moved to their new positions by a small amount along the forces. At this point, the ground state density is perturbed and must be recalculated in a self-consistent field step as described above. This process continues until a treshold is achieved for the force acting on each atom.

At the end of the calculation, resultant positions of atoms, magnetization, total energy of the system and several information is given in an output file. Other information which will be used for further analysis, such as the real space wavefunctions, density, and effective potential are stored in binary format in a separate directory.

2.6.2 Bader Charge Analysis

The electronic charge distribution in a system fails to desribe the atomic charges present in a molecule or solid [47]. The Kohn-Sham equations are constructed by continuous electron densities, therefore quantum mechanically it is not possible to deduce the charge properties of distinct atoms. In Bader charge analysis, the space is divided into small regions by surfaces. On each surface the charge

density should be minimum perpendicular to the surface, which is called zero flux surface [48]. When the minima occurs, a zero flux surface divides the region between atoms, and each atom would have its own space. Since the idea is based on charge density, the choice of the basis set is not relevant with the Bader charge analysis. Therefore it is compatible with the output results obtained by DFT calculations.

2.6.3 d-Band Structure

Due to the complexity of consecutive reactions during a combustion process, it is essential to understand the electronic properties of heterogeneous catalysts [49]. A number of descriptors are being used for this purpose, which enlighten the favourable geometries and atomic sites of the alloy structure. One of the key concepts for transition metal alloys is d-band analysis.

The d states form relatively narrow energy bands due to the small coupling matrix element V_{dd} between the localized d states, which give rise to the formation of bonding and antibonding states by surface electrons [50]. As the center of d band ϵ_d increase in terms of energy, the band width decrease which causes distinctive antibonding states above the Fermi energy level. The antibonding states located above the Fermi energy level are not occupied, therefore their weakinging effects disappear, which causes stronger chemical bonds. In other words, antibonding states mostly located above (below) Fermi energy level, ϵ_F, causes stronger (weaker) bonds. Here, the d-band center is the first moment of partial DOS of d orbitals, and is calculated as

$$\epsilon_d = \frac{\int E N_d(E) dE}{\int N_d(E) dE}. \tag{2.58}$$

In addition to the d-band center ϵ_d, d-band width ω_d is a valuable descriptor for the surface activity, which is the second moment of the partial DOS of d orbitals. The width of d-band ω_d is also strongly related with the formation of antibonding states:

$$\omega_d = 4\sqrt{\frac{\int (E-\epsilon_d)^2 N_d(E) dE}{\int N_d(E) dE}}. \tag{2.59}$$

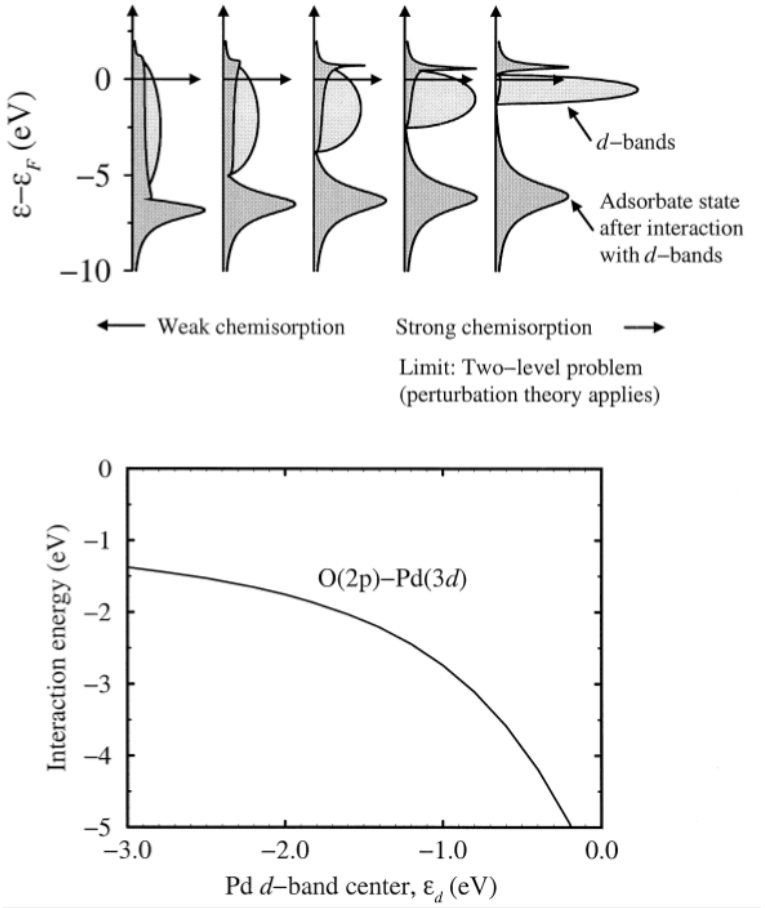

Figure 2.2: PDOS of an interaction between the surface d bands and an adsorbate state. Number of electrons in the band kept constant by stabilizing the strength of coupling matrix element V and decreasing the width W of d bands. Reprinted from Hammer [51] .

One last descriptor related to d-band theory is the d band *edge* [52], μ_d, which is the highest peak position of the Hilbert transform of the density of d states. μ_d is calculated by

$$\mu_d = \arg\max \frac{1}{\pi} P \int_{-\infty}^{\infty} \frac{\rho(\epsilon')}{\epsilon - \epsilon'} d\epsilon'. \tag{2.60}$$

CHAPTER 3

RESULTS AND DISCUSSION

In this chapter, adsorption properties and geometry of ethanol molecule (C_2H_6O) over (111) surfaces of Au with dopants (Ni, Rh) are investigated after observing the properties of bulk and bare (111) surface of Au with dopants (Ni, Rh). Through the whole study PDOS, d-band and Bader charge analyses are done for each structure to understand the phenomena behind the process. The calculations are done using the Quantum Espresso package, in which DFT is implemented [45]. The variant of GGA developed by Perdew-Burke-Ernzerhof (PBE) is used throughout the thesis. The interaction of valence electrons with atomic core states is described by ultrasoft pseudopotentials.

3.1 Bulk Structure

Bulk Au has a face centered cubic structure (a=b=c, $\alpha = \beta = \gamma$). Cell parameters are obtained after the optimization of parameters by convergence calculations. Cutoff energy for plane wave basis is found as 40 Ry, while the determined augmented electron density value is 400 Ry. In the relaxation calculation $16 \times 16 \times 16$ k-point mesh grid has been used. The cell parameters of pure bulk Au is found to be 7.89 Å, which is 2.63 % higher then the value in the literature [32].

After obtaining the lattice constant for pure bulk Au, five different concentrations of dopant atoms in the bulk structure have been studied, namely AuX_1, AuX_2, AuX_4, AuX_8, AuX_{16} (Fig. 3.1 & Fig. 3.2). The subscript beneath each

dopant indicates the number of dopant in the bulk. To be able to examine a large scale of concentration percentage, the supercell is chosen as 4×4 unit cells with 4 layers, containing 32 atoms. The elements Ni and Rh are used for alloying, which also have the same Bravais lattice type. Properties of these bulk structures have been studied to understand the effects of dopant to the structural and electronic properties of the bulk Au, moving on to the surface calculations.

Lattice constant and cohesive energy of these concentrations are examined with and without considering spin. As seen in Table 3.1, lattice constant and cohesive energy of doped bulk Au gradually increases as expected. The lattice mismatch between Au and dopant is not in a considerable range at low concentrations. Therefore lattice strain will not be considered as a surface reaction modifier. Magnetization in the spin-polarized case is invoked only in high concentrations, which is more significant in Rh-doped bulk alloys. For further calculations, spinless calculations will not be used, since they do not perform any significant difference from spin-polarized case. The results of partial density of states analysis (PDOS) are presented in Fig. 3.3 & Fig. 3.4.

As seen in Fig. 3.3, the number of d states due to the contribution of dopant elements increases significantly. In the case of the AuNi alloy, number of d states of Ni increase sharply just above the Fermi energy level up to 25 % concentration ($AuNi_8$). For the case of 50 % concentration ($AuNi_{16}$) the shape of d band broadens, instead of exhibiting a sharp peek, with a little percentage above the Fermi level. However, until 50 % concentration of dopant, antibonding states are oriented just below the Fermi energy level, which indicates that AuNi alloy may not perform high catalytic activitiy, according to the d band theory. As the concentration of the dopant increases, the d band contribution of Au decrease, while having smaller but sharper peaks.

In the case of AuRh alloy, we observe relatively smaller peaks in the shape of d states of dopant element up to 25 % percent ($AuRh_8$). However, in this case, the d states in $AuRh_8$ located above the Fermi level with a small amount, which causes an increase in the activty of the structure.

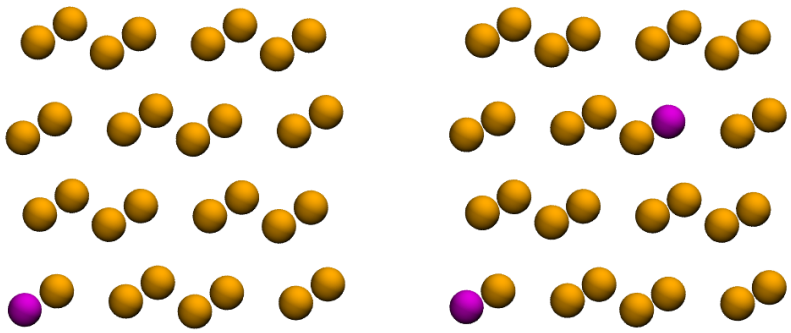

(a)

(b)

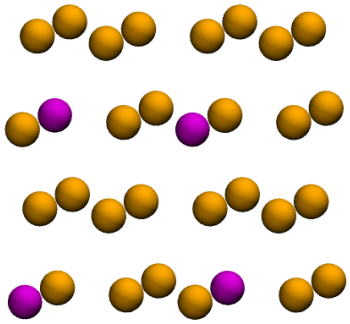

(c)

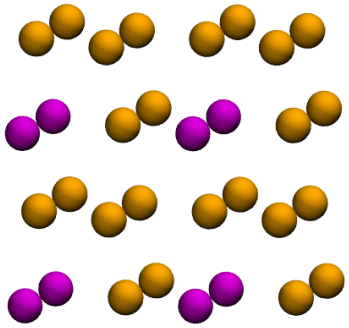

(d)

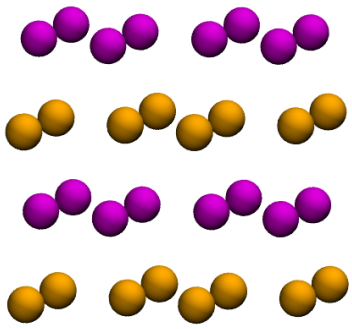

(e)

Figure 3.1: Various concentrations of Ni dopant in Au Bulk structures.These are, respectively, $AuNi_1$, $AuNi_2$, $AuNi_4$, $AuNi_8$, $AuNi_{16}$

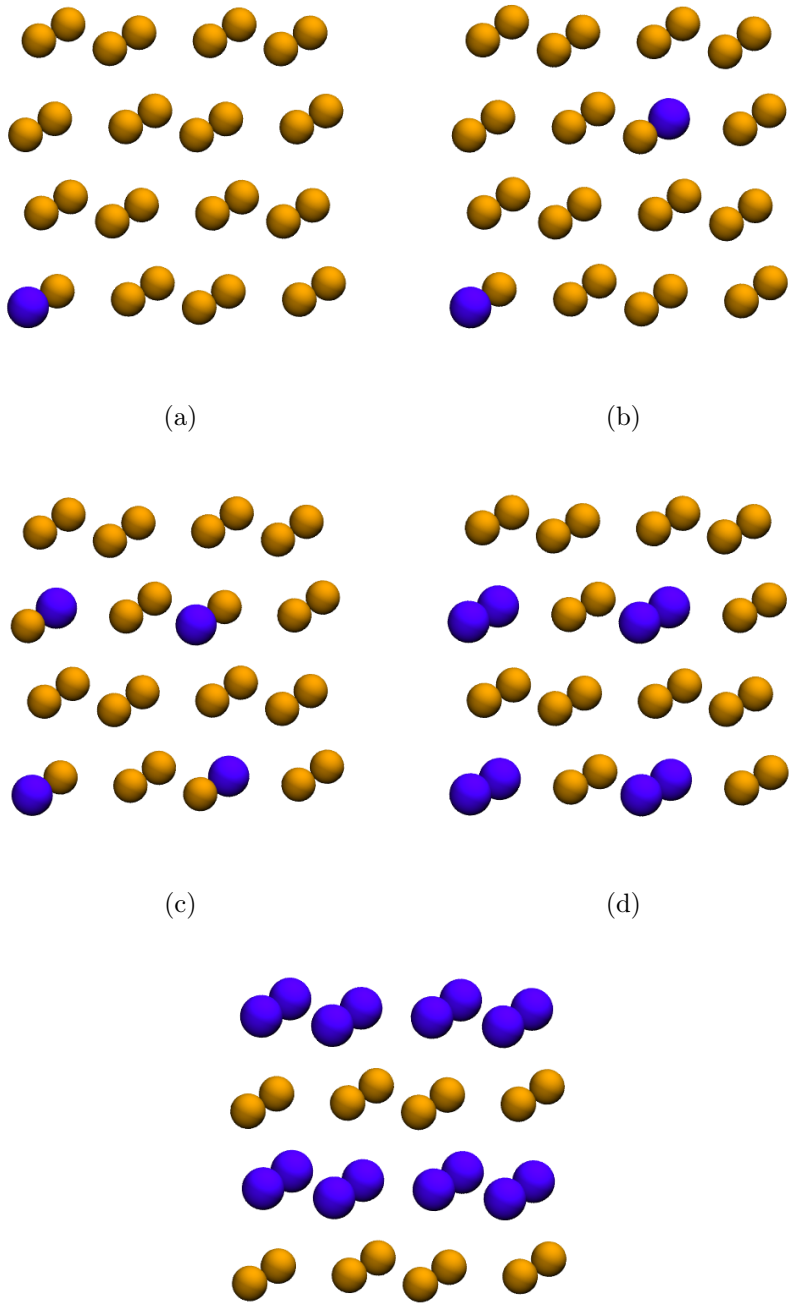

(a) (b) (c) (d) (e)

Figure 3.2: Various concentrations of Rh dopant in Au Bulk structures.These are, respectively, $AuRh_1$, $AuRh_2$, $AuRh_4$, $AuRh_8$, $AuRh_{16}$.

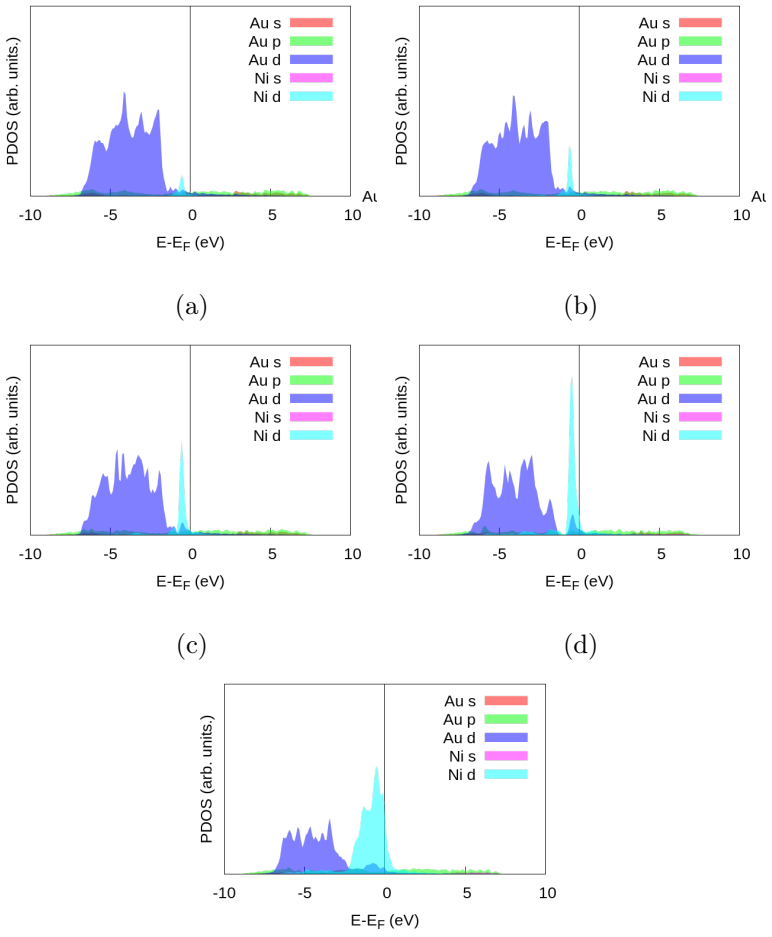

Figure 3.3: PDOS plots of various concentrations of Ni dopant in Au Bulk structures with respect to increasing concentrations from $AuNi_1$ to $AuNi_{16}$

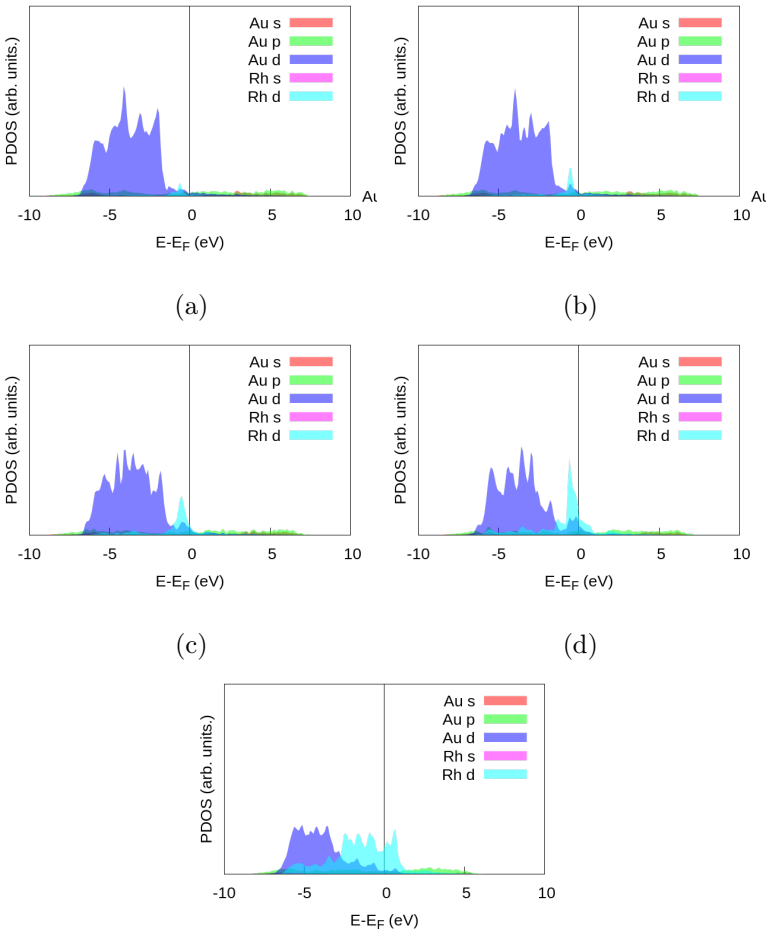

Figure 3.4: PDOS plots of various concentrations of Rh dopant in Au Bulk structures with respect to increasing concentrations from $AuRh_1$ to $AuRh_{16}$

Table3.1: Lattice constant (in Bohr), cohesive energy (in eV/atom) and magnetization (μ) (in Bohr mag/cell) values of bulk unit cells. The change of lattice constant with respect to the pure bulk is given in parantheses.

	Spin Unpolorized		Spin Polorized		
Bulk	Lattice Const.	Cohesive E.	Lattice Const.	Cohesive E.	μ
$AuNi_1$	7.87 (0.42 %)	-3.04	7.86 (0.39 %)	-3.20	0.01/0.01
$AuNi_2$	7.84 (0.76 %)	-3.09	7.83 (0.78 %)	-3.26	0.00/0.00
$AuNi_4$	7.78 (1.54 %)	-3.16	7.77 (1.54 %)	-3.37	0.00/0.00
$AuNi_8$	7.63 (3.35 %)	-3.36	7.62 (3.35 %)	-3.63	0.98/1.27
$AuNi_{16}$	7.34 (7.10 %)	-3.78	7.33 (7.03 %)	-4.18	6.28/7.25
$AuRh_1$	7.88(0.29 %)	-3.07	7.87 (0.29 %)	-3.22	0.00/0.01
$AuRh_2$	7.86 (0.50 %)	-3.13	7.85 (0.50 %)	-3.31	0.00/0.00
$AuRh_4$	7.82 (0.98 %)	-3.25	7.81 (0.97 %)	-3.46	1.18/1.53
$AuRh_8$	7.76 (1.86 %)	-3.50	7.76 (1.64 %)	-3.78	7.57/9.20
$AuRh_{16}$	7.67 (3.71 %)	-4.19	7.67 (2.83 %)	-4.60	24.08/28.09

Moreover, the width of d states is broader but smaller than the one in AuNi alloy. Additionally, the number of d states that belong to dopant element in AuRh alloys is always smaller than the number of d states of Au atoms, while d states of Ni become dominant as the concentration incerase. For a better understanding, the numerical values of d-band center ϵ_d and d-band width ω_w are calculated by considering all atoms in the unit cell, by using Eq. 2.58 and Eq. 2.59. The results are represented in Table 3.2.

According to these results, Rh appears more favorable for surface activation than Ni in the case of their Au alloys. However, there does not seem to be a link between the dopant concentration and d-band center shift.

In addition to PDOS analysis we have conducted Bader charge analysis, which is essentialy a method of analysing the electronic charge density per atom of a crystal structure, by means of dividing space into atomic volumes. The partial charge values on the dopant atom results for all bulk structures presented in

Table3.2: D-Band center (ϵ_d) and width (ω_d) values for both AuNi and AuRh alloys in [eV].

Bulk	ϵ_d(Au-Ni/Rh)	ω_d(Au-Ni/Rh)
Au	-3.66	120.16
$AuNi_1$	-3.66 - -0.70	13.09 - 13.96
$AuNi_2$	-3.67 - -0.74	13.06 - 14.35
$AuNi_4$	-3.67 - -0.61	13.01 - 14.59
$AuNi_8$	-3.76 - -0.58	12.94 - 14.70
$AuNi_{16}$	-4.08 - -0.86	12.72 - 14.60
$AuRh_1$	-3.63 - -1.10	13.14 - 13.77
$AuRh_2$	-3.53 - -0.73	13.13 - 14.21
$AuRh_4$	-3.52 - -0.83	13.14 - 14.50
$AuRh_8$	-3.52 - -0.86	13.09 - 14.55
$AuRh_{16}$	-3.91 - -1.44	12.98 - 14.40

Table 3.3. In the case of AuNi alloys, Ni atoms release ~ 0.35 electrons to the surrounding Au atoms in all concentrations. On the other hand, in the case of AuRh alloys, in 12.5 % and 25 % concentrations, Rh atoms tend to donate less electrons (~ 0.1) to the surrounding Au atoms, while in other three concentrations, each Rh atom release ~ 0.35 electrons.

3.2 Surface Calculations

Ethanol is being used as a constituent molecule for the production of precious materials for various industries. Therefore it has been a widely studied topic in catalysis studies [2]. To be able to determine the affects of catalytic surface to reaction pathway, it is important to investigate the interaction between the reactant, ethanol in our case; and products with the surface.

Table3.3: Charge donation by dopant atoms according to Bader partitioning in [|e|].

	Charge
$AuNi_1$	+ 0.35
$AuNi_2$	+ 0.35
$AuNi_4$	+ 0.35
$AuNi_8$	+ 0.35
$AuNi_{16}$	+ 0.35
$AuRh_1$	+ 0.30
$AuRh_2$	+ 0.30
$AuRh_4$	+ 0.10
$AuRh_8$	+ 0.10
$AuRh_{16}$	+ 0.35

Table3.4: Atomic displacement of dopant atom and magnetization of the system.

Structure	Atomic Displacement (Å)	μ (Bohr mag/cell)
AuNi	0.32	0.90
AuRh	0.29	1.77

3.2.1 Bare Surface Calculations

Both structural and electronic properties of the same material show different properties with respect to the Miller index of the material. In the same manner, these properties differ as the surface structure changes. In this work, the properties of (111) surface of Au with a single dopant (Ni, Rh) on the surface has been studied. For the surface calculations, a 3×3 surface slab with 5 layers was used. The value of kinetic energy cutoff is the same with bulk structure calculations (40 Ry), while $4 \times 4 \times 1$ k-point mesh grid have been used. In the calculations the two bottom layers were held fixed to mimic bulk behavior. The infinite surface is created by the software, by laterally replicating the unit cells. A vacuum distance of ~ 17Å introduced to avoid interaction between the created unit cell in z-direction, which is perpendicular to the surface plane.

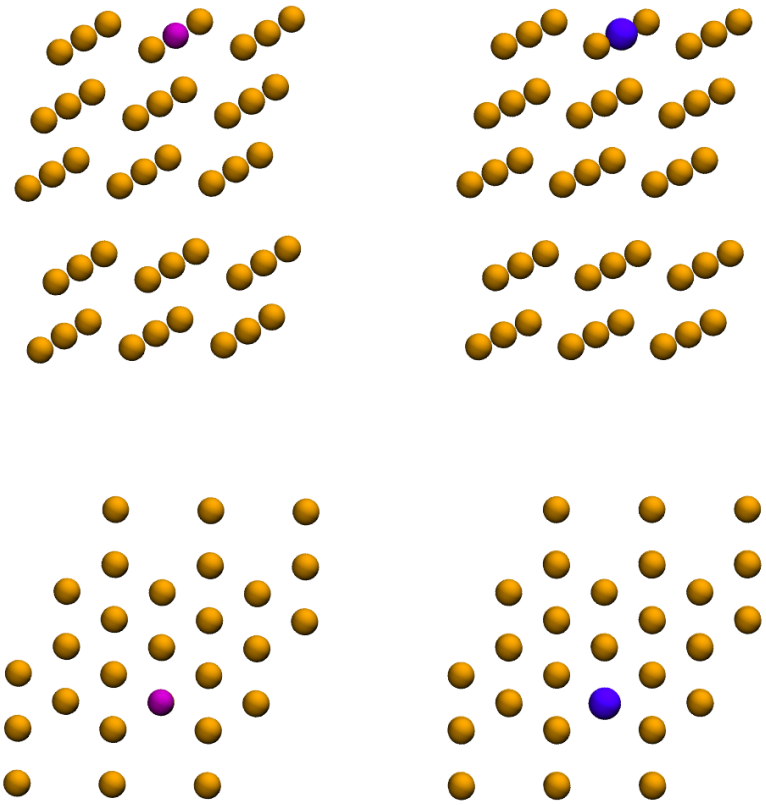

(a) (b)

Figure 3.5: Side and top view of (111) AuNi alloys on the left side and AuRh alloys on the right side.

The central Au atom of the top layer is substituted with a Ni/Rh atom (Fig. 3.5). After geometry optimization, Ni and Rh atom are observed to sink surface (see Fig. 3.6) due to their smaller size. Due to the dopants, a considerable amount of magnetization occurs inside the structures.

PDOS analysis of these structures does not show significant difference from the bulk for single dopant (see Fig. 3.7). On the other hand, d-band properties of dopant atoms show considerable changes (Table 3.5). D-band center associated with the Ni atom shifts ~ 0.1 eV higher, indicating that its activity is increased when moved from bulk to surface. Center of d-band associated with Rh atom, in the other structure, show even more increase and shifts ~ 0.3 eV through Fermi level.

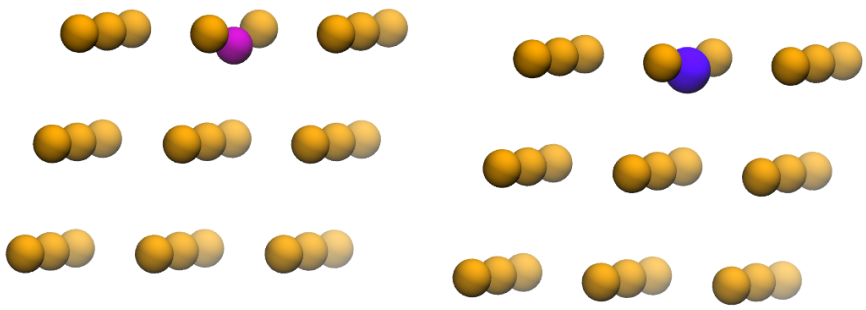

(a) (b)

Figure 3.6: Both Ni and Rh dopants burried into surface by 0.32 Å and 0.1 Å respectively.

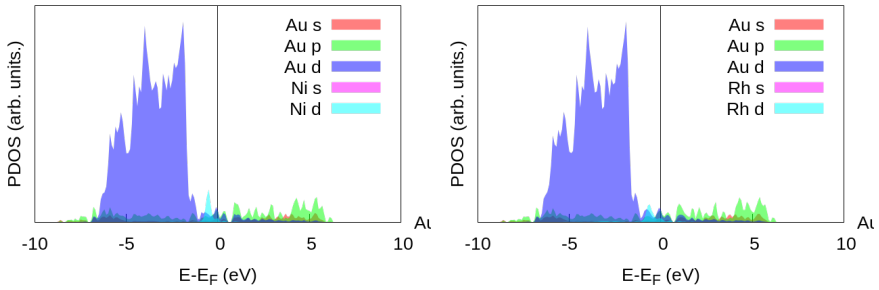

Figure 3.7: PDOS of a: AuNi surface alloy, b: AuRh surface alloy

Table3.5: D-band center and width values of surface dopants in [eV]. atoms

	AuNi		AuRh	
Atom	ϵ_d	ω_d	ϵ_d	ω_d]
Au	-3.12	2.65	-3.08	2.87
X	-0.62	6.46	-0.87	6.23

Table3.6: Bader charge analysis of (111) Au surfaces with a single dopant and its nearest neighbors on the surface in [|e|].

AuNi		AuRh	
Atom	Charge	Atom	Charge
Au	-0.05	Au	-0.04
Au	-0.08	Au	-0.07
Au	-0.08	Au	-0.06
Ni	+0.34	Rh	+0.15
Au	-0.06	Au	-0.04
Au	-0.07	Au	-0.05
Au	-0.09	Au	-0.07

Intuitively, we expect that active sites in both cases will be located around the dopant atoms. Bader charge analysis (Table 3.6) indicates that dopant atoms grant their charge to neighboring Au atoms on the surface. Hence, it becomes negatively charged, which makes it more active than the surrounding Au atoms. Both the increase in d-band centers of dopant atoms ϵ_d and Bader charge analysis indicats that Ni and Rh can be effective candidates for surface modification.

3.2.2 Adsorption of Ethanol on AuNi and AuRh Surfaces

In order to identify the interaction between the surface and the molecule, we have invesetigated the adsorption of ethanol through surface. In this study, we have investigated each reaction step on five different lattice sites to find energically most favourable position for the adsorption ethanol molecule. The *active site* is the position on the surface, where the probabilty of adsorption of molecule is higher than other locations on the surface. There are five different active sites on the (111) surface of an fcc structured crystal. These lattice sites are namely bcc, two different bridge sites (bridge_1 & bridge_2), fcc and ontop (Fig. 3.8).

After relaxation of each system, binding energy and bond lenght of adsorption has been investigated (Table 3.7). For the Ni doped surface, top of the Ni atom,

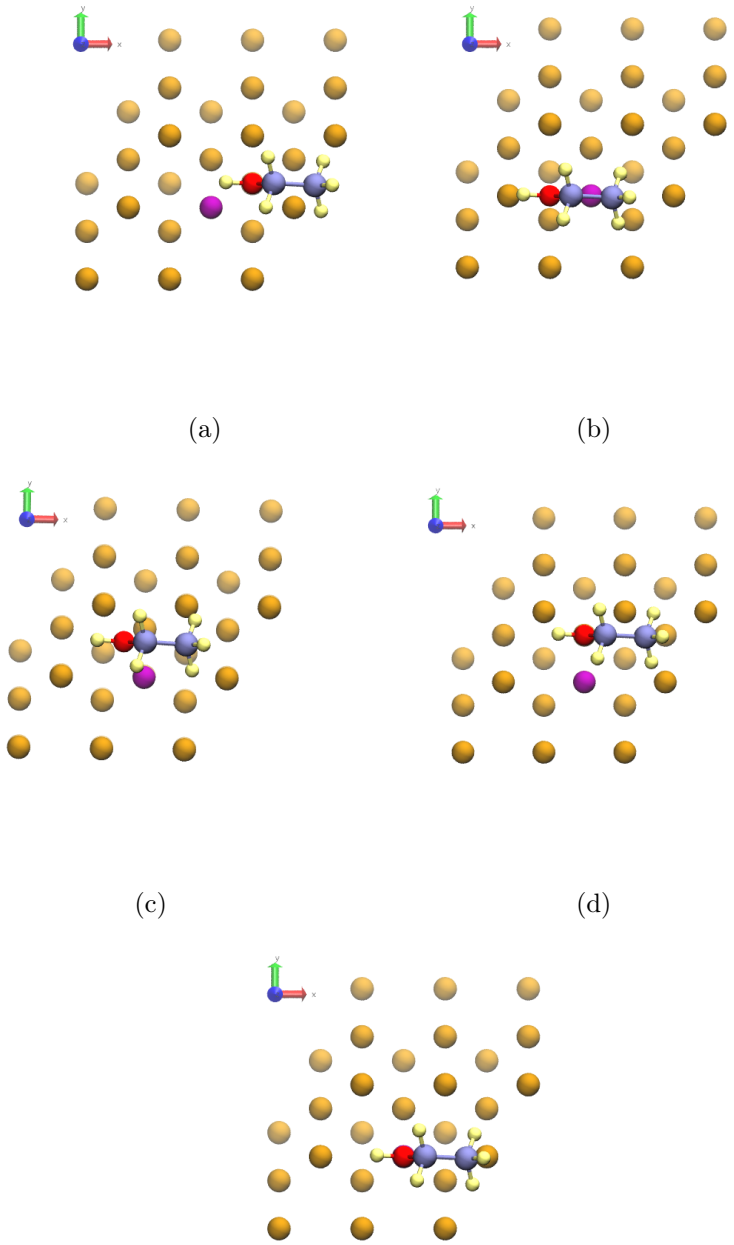

Figure 3.8: Ethanol molecule placed on five different lattice sites of (111) Au surface. Starting from left top: a) bcc, b) bridge_1, c) bridge_2, d) fcc, e) ontop.

Table3.7: Binding energy and bond length of ethanol adsorption on different surface sites.

AuNi			AuRh		
Lattice Site	E_{ad} [eV]	d_{ad} [Å]	Lattice Site	E_{ad} [eV]	d_{ad} [Å]
bcc	-0.11	3.74	bcc	-0.11	3.66
$bridge_1$	-0.49	2.10	$bridge_1$	-0.55	2.25
$bridge_2$	-0.48	2.09	$bridge_2$	-0.54	2.24
fcc	-0.13	3.16	fcc	-0.55	2.25
ontop	-0.49	2.08	ontop	-0.75	2.36

also the bridge sites seem to be more favourable than bcc and fcc sites. Similarly, top of Rh atom energetically more favourable than other sites. However, fcc site seems to bind ethanol molecule with a shorter bond. Nevertheless, all sites of AuRh surface seems to be a potential binding position, except bcc site.

Results of Bader charge analysis of ethanol adsorbed surfaces are in good agreement with the results presented in Table 3.7. O atom collects charge from other atoms of the molecule in all cases. Moreover, the change in charge of dopant atoms is more significant in the surface sites, which are mentioned as *more favourable* (see Table 3.8). However, d-band center results contradicts with the theory. For example, in AuNi case, bcc and fcc sites are indicated as *least favourable sites*. However, as seen in Table 3.9, the dopant atoms in these surface sites has the highest d band center values, which means they are more favourable, according to the theory. On the other hand, their d-band width is narrower than the other sites, which is a result that follows the theory.

In the case of AuRh, similar contradictions are seen. Ontop position was mentioned to be one of the active sites on AuRh surface. However, it has the lowest d-band center value, which is a downside, according to the theory. Additionally, it has the most narrow d-band width. Hence, these two descriptors are not reflecting the surface activity in our case.

Table3.8: Charge difference of atoms with -O bond and surface dopant atom after the adsorption process in [|e|]. Other atoms in the molecule are omitted, since the change in their charge is negligable.

Atom	bcc	$bridge_1$	$bridge_2$	fcc	ontop
Ni	+0.35	+0.47	+0.47	+0.38	+0.47
C	+0.69	+0.61	+0.53	+0.67	+0.58
O	-1.73	-1.64	-1.64	-1.72	-1.65
H	+1.00	+1.00	+1.00	+1.00	+1.00
Rh	+0.17	+0.32	+0.30	+0.32	+0.45
C	+0.61	+0.55	+0.58	+0.51	+0.51
O	-1.71	-1.62	-1.62	-1.61	-1.65
H	+1.00	+1.00	+1.00	+1.00	+1.00

Table3.9: D-band properties of ethanol adsorbed AuNi and AuRh surfaces in [eV].

	ϵ_d		ω_d		μ_d
Structure	Au	Ni/Rh	Au	Ni/Rh	Ni/Rh
$AuNi_{bcc}$	-3.14	-0.61	2.65	6.82	3.65
$AuNi_{bridge1}$	-3.17	-0.75	2.75	6.73	3.55
$AuNi_{bridge2}$	-3.18	-0.76	2.74	6.73	2.59
$AuNi_{fcc}$	-3.14	-0.61	2.62	6.80	3.58
$AuNi_{ontop}$	-3.18	-0.77	2.73	6.70	3.60
$AuRh_{bcc}$	-3.16	-0.87	3.01	6.49	3.58
$AuRh_{bridge1}$	-3.15	-1.04	3.11	6.35	3.49
$AuRh_{bridge2}$	-3.11	-1.05	3.11	6.33	3.48
$AuRh_{fcc}$	-3.10	-1.03	3.10	6.35	3.50
$AuRh_{ontop}$	-3.20	-1.97	3.08	4.89	2.63

Table3.10: Binding energy and bond length of ethoxy adsorption on different surface sites.

AuNi			AuRh		
Lattice Site	E_{ad} [eV]	d_{ad} [Å]	Lattice Site	E_{ad} [eV]	d_{ad} [Å]
bcc	-2.38	1.90	bcc	-2.24	2.15
$bridge_1$	-2.34	1.89	$bridge_1$	-2.11	1.99
$bridge_2$	-2.36	1.89	$bridge_2$	-2.30	1.97
fcc	-2.38	1.89	fcc	-2.32	1.97
ontop	-2.32	1.88	ontop	-2.31	1.97

3.2.3 Adsorption of Ethoxy on AuNi and AuRh Surfaces

Investigating the interaction between the surface and the desired product is an essential step for defining a reasonable reaction pathway. In our case the product, ethoxy, is obtained by breaking the O-H bond. The aim of this work is achieving the reaction in Eq. 3.1 by surface alloying, instead of using pre-oxygen covered catalyst surface.

$$CH_3CH_2OH \longrightarrow CH_3CH_2O^* + H^* \tag{3.1}$$

As seen in Table 3.10, the adsorption properties of ethoxy are greater than the ones of ethanol, since the O in molecule has one less bond. In contrast to the ethanol case, there is no preferential surface site for the adsorption of ethoxy in both AuNi and AuRh surfaces.

Similarly, d-band and Bader charge analyses have shown monotonic results for the adsorption over AuNi surface. On the other hand, d-band center of Rh has higher values in bcc and $bridge_2$ surface sites. Yet, the differences do not lead to a conclusion for the preferability of the sites.

3.2.4 Adsorption of H on AuNi and AuRh Surfaces

After the reaction takes place, H radical will remain on the surface long enough to affect the adsorption mechanism of the product. In this sense, adsorption of

Table3.11: D-band properties of ethoxy adsorbed AuNi and AuRh surfaces in [eV].

	ϵ_d		ω_d		μ_d
Structure	Au	Ni/Rh	Au	Ni/Rh	Ni/Rh
$AuNi_{bcc}$	-3.18	-0.89	2.52	6.35	3.56
$AuNi_{bridge1}$	-3.18	-0.89	2.50	6.34	3.53
$AuNi_{bridge2}$	-3.18	-0.90	2.50	6.32	3.51
$AuNi_{fcc}$	-3.18	-0.90	2.13	9.05	3.48
$AuNi_{ontop}$	-3.18	-0.92	2.50	6.30	3.47
$AuRh_{bcc}$	-3.23	-0.98	2.57	6.33	4.34
$AuRh_{bridge1}$	-3.11	-1.3	2.62	5.70	3.27
$AuRh_{bridge2}$	-3.12	-0.87	2.49	6.21	3.19
$AuRh_{fcc}$	-3.10	-1.35	2.52	5.52	3.17
$AuRh_{ontop}$	-3.11	-1.36	2.52	5.52	3.18

Table3.12: Charge difference of atoms O and C, and surface dopant atom after the adsorption process in [|e|]. Other atoms in the molecule are omitted, since the change in their charge is negligable.

Atom	bcc	$bridge_1$	$bridge_2$	fcc	ontop
Ni	+0.53	+0.54	+0.53	+0.53	+0.54
C	+0.63	+0.68	+0.54	+0.58	+0.63
O	-1.18	-1.18	-1.18c	-1.18cd	-1.19cd
Rh	+0.54	+0.45	+0.49	+0.47	+0.48
C	+0.62	+0.73	+0.76	+0.75	+0.73
O	-1.20	-1.18	-1.17	-1.16	-1.15

Table3.13: Binding energy and bond length of ethoxy adsorption on different surface sites.

AuNi			AuRh		
Lattice Site	E_{ad} (eV)	d_{ad} (Å)	Lattice Site	E_{ad} (eV)	d_{ad} (Å)
bcc	-3.51	1.66	bcc	-3.69	1.71
$bridge_1$	-3.46	1.60	$bridge_1$	-3.67	1.66
$bridge_2$	-3.46	1.60	$bridge_2$	-3.67	1.66
fcc	-3.49	1.65	fcc	-3.69	1.69
ontop	-3.25	1.47	ontop	-3.60	1.57

Table3.14: Charge difference of H atom and surface dopant atom after the adsorption process in [|e|].

Atom	bcc	$bridge_1$	$bridge_2$	fcc	ontop
Ni	+0.37	+0.37	+0.37	+0.37	+0.36
H	-0.15	-0.13	-0.15	-0.14	-0.14
Rh	+0.54	+0.45	+0.49	+0.47	+0.48
H	-1.20	-1.18	-1.17	-1.16	-1.15

atomic H has been calculated before moving on to the calculation of real event , in which adsorption of both ethoxy and h on the same surface is calculated (Table 3.13).

As one would expect, H radical sinks surface with relatively high binding energy. Bader charge analysis show that H radical gets negatively charged and attacted by the positively charged surface dopant. Bader charge analyses shows that adsorption properties of atomic H does not vary with respect to the surface site.

3.2.5 Adsorption of H and Ethoxy on AuNi and AuRh Surfaces

Seperate calculations of the adsorption of products showed that once the H-O bond is broken, both H and ethoxy tend to bind to surface without any distinct surface lattice preferences. However it is essential to determine the final stage of

Table3.15: Binding energy and bond length of both H and ethoxy adsorption on specified surface sites .

Structure	E_{ad} [eV]	d_{H-X} [Å]	d_{O-X}[Å]
AuNi	-5.80	1.63	1.93
AuRh	-5.82	1.70	2.00

both products for defining the reaction pathway. Using the previous calculations, we have performed the adsorption calculations for possible results of oxidation of ethanol over doped (111) Au surfaces.

In the AuNi case, H atom placed in the middle of the $bridge_1$ and $bridge_2$ sites, while ethoxy molecule placed at fcc surface site. In the AuRh case, H atom placed at fcc lattice site instead of ethoxy, while the molecule placed at the top of Rh atom (Fig. 3.9).

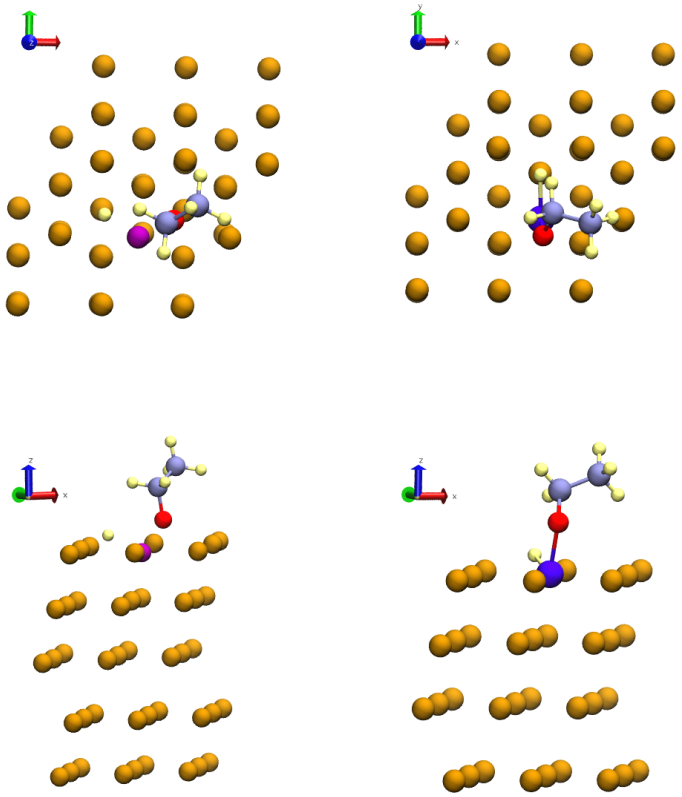

(a) (b)

Figure 3.9: Top and side view of the position of H and ethoxy over a) AuNi surface alloy and b) AuRh surface alloy

CHAPTER 4

CONCLUSION

Increasing need of syntethetic chemicals for various industries necessitates new production methods in order to reduce the pollution factors. With this motivartion, numerous catalytic materials have been develoed. Au based catalytic surfaces are gathering the most attention among these catalysts, however, activation of Au surfaces is achieved by pre-oxidation of the surface, which is a costly method. An alternative strategy to increase the surface activity of Au catalysts is alloying with transtion metals. In this thesis Ni and Rh doped (111) Au surfaces were investigated as a candidate catalyst for selective oxidation of ethanol.

Preliminary calculations are done to obtain reliable parameters which have been used in the calculations, such as lattice constants, cutoff energy for the plane wave basis and k-point meshes.

Starting from the bulk structures of different concentrations of dopant atom, we have investigated the affects of dopant atom to the mechanical and electronic properties of bulk. Lattice mismatch due to the dopant is significat only in the high concentration Ni doped case. Therefore lattice strain is not considered as a reliable reaction modifier in the frame of this study. Calculated d-band values are not in coherence with the increasing dopant percentage, however the charge transfer between the dopant and surface atoms is considerably high.

Calculated binding energies of ethanol shows that chemically inert (111) Au surface become slightly active with the low concentration of dopant in both cases.

Rh doped surface is more favourable than the Ni doped surface. Adsorption of ethoxh and H results also shows that AuRh alloy is a promising candidate as a catalyst for the selective oxidation of ethanol. Through all adsorption energy calculations, charge transfer between the dopant and surface atoms is a valid explanation for the formation of the bond between the adsorbate and the surface. On the other hand, d-band values do not show the same trend with the binding energies, as stated in the theory. Considering all reaction modifiers, charge transfer between dopant and surface atoms is more successful than the other reaction modifiers.

In both Ni and Rh doped (111) Au surfaces, activation of the surface has been achived with small binding energies. Increasing the concentration of dopant on the surface with a larger unit cell may reduce the activation barrier for the selective oxidation of ethanol on (111) Au surfaces.

REFERENCES

[1] The European Chemical Industry Council. `http://fr.zone-secure.net/13451/186036/?startPage=3#page=3`. last visited on July 2016.

[2] Y. Guan and E.J.M. Hensen. Selective oxidation of ethanol to acetaldehyde by Au-Ir catalysts. *Journal of Catalysis*, 305:135 – 145, 2013.

[3] P. J. Chenier. *Survey of Industrial Chemistry*. Kluwer Academic/Plenum, 233 Spring Street, New York, N.Y. 10013, 2002.

[4] Climate Change 2013: The Physical Science Basis. `http://www.climatechange2013.org/images/report`. last visited on July 2016.

[5] N. Raveendran Shiju and V. V. Guliants. Recent developments in catalysis using nanostructured materials. *Applied Catalysis A: General*, 356(1):1 – 17, 2009.

[6] T. Asefa, M. J. MacLachlan, Neil Coombs, and G. A. Ozin. Periodic mesoporous organosilicas with organic groups inside the channel walls. *Nature*, 402(6764):867–871, 1999.

[7] Q. Yang, Y. Li, L. Zhang, J. Yang, J. Liu, and C. Li. Hydrothermal stability and catalytic activity of aluminum-containing mesoporous ethane silicas. *The Journal of Physical Chemistry B*, 108(23):7934–7937, 2004.

[8] S. C. Shen and S. Kawi. MCM-41 with improved hydrothermal stability: Formation and Prevention of Al content dependent structural defects. *Langmuir*, 18(12):4720–4728, 2002.

[9] M. A. Wahab and Chang-Sik Ha. Ruthenium-functionalised hybrid periodic mesoporous organosilicas: Synthesis and structural characterization. *J. Mater. Chem.*, 15:508–516, 2005.

[10] J. Xiang, P. Wang, S. Su, L. Zhang, F. Cao, Z. Sun, Xi Xiao, L. Sun, and S. Hu. Control of NO and Hg^0 emissions by SCR catalysts from coal-fired boiler. *Fuel Processing Technology*, 135:168 – 173, 2015. 2014 Australia-China Symposium on Energy.

[11] D. Loffreda, C. Michel, F. Delbecq, and P. Sautet. Tuning catalytic reactivity on metal surfaces: Insights from DFT. *Journal of Catalysis*, 308:374 – 385, 2013.

[12] N. P. Cheremisinoff. *Handbook of Industrial Toxicology and Hazardous Materials*. Marcel Dekker, Inc., 270 Madison Avenue, New York, NY 10016, 1999.

[13] S. X. Liu, L. W. Liao, Q. Tao, Y. X. Chen, and S. Ye. The kinetics of CO pathway in methanol oxidation at Pt electrodes, a quantitative study by ATR-FTIR spectroscopy. *Physical Chemistry Chemical Physics*, 13:9725–9735, 2011.

[14] Francesca Cardona and Camilla Parmeggiani, editors. *Transition Metal Catalysis in Aerobic Alcohol Oxidation*. The Royal Society of Chemistry, Thomas Graham House, Science Park, Milton Road, Cambridge CB4 0WF, UK, 2015.

[15] Q. Meng, Y. Shen, J. Xu, and J. Gong. Mechanistic insights into selective oxidation of ethanol on au(111): A DFT study. *Chinese Journal of Catalysis*, 33(23):407 – 415, 2012.

[16] B. Xu, X. Liu, J. Haubrich, and C. M. Friend. Vapour-phase gold-surface-mediated coupling of aldehydes with methanol. *Nature chemistry*, 2(1):61–5, 2010.

[17] C. P. Vinod, K. Wilson, and A. F. Lee. Recent advances in the heterogeneously catalysed aerobic selective oxidation of alcohols. *Journal of Chemical Technology and Biotechnology*, 86:161–171, 2011.

[18] Q. Meng, Y. Shen, Jing Xu, Xinbin Ma, and Jinlong Gong. Mechanistic understanding of hydrogenation of acetaldehyde on Au(111): A DFT investigation. *Surface Science*, 606:1608–1617, 2012.

[19] T. Nishimura, T.i Onoue, K. Ohe, and S. Uemura. Palladium(ii)-catalyzed oxidation of alcohols to aldehydes and ketones by molecular oxygen. *The Journal of Organic Chemistry*, 64(18):6750–6755, 1999. PMID: 11674682.

[20] H. J. Sedjame, C. Fontaine, G. Lafaye, and J. Barbier Jr. On the promoting effect of the addition of ceria to platinum based alumina catalysts for VOCs oxidation. *Applied Catalysis B: Environmental*, 144:233 – 242, 2014.

[21] X. Chen. Exotemplated copper, cobalt, iron, lanthanum and nickel oxides for catalytic oxidation of ethyl acetate. *Journal of Environmental Chemical Engineering*, 1(4):795 – 804, 2013.

[22] M. Haruta, N. Yamada, T. Kobayashi, and S. Iijima. Gold catalysts prepared by coprecipitation for low-temperature oxidation of hydrogen and of carbon monoxide. *Journal of Catalysis*, 115:301–309, 1989.

[23] S. Jalili, A. Zeini Isfahani, and R. Habibpour. Atomic oxygen adsorption on Au (100) and bimetallic Au/M (M = Pt and Cu) surfaces. *Computational and Theoretical Chemistry*, 989:18 – 26, 2012.

[24] D.W. Yuan, Z.R. Liu, and Y. Xu. First-principles investigations of O_2 dissociation on low-coordinated pd ensembles over stepped au surfaces. *Physics Letters A*, 376(45):3432 – 3438, 2012.

[25] I. X. Green, M. McEntee, W. Tang, M. Neurock, and J. T. Yates. Direct formation of acetate from the partial oxidation of ethylene on a Au/TiO_2 catalyst. *Topics in Catalysis*, 56(15):1512–1524, 2013.

[26] L. M. C. Pinto and G. Mai. Oxygen adsorption on PdPt/Au(111) DFT calculations. *The Journal of Physical Chemistry C*, 119(15):8213–8216, 2015.

[27] W. Y. Yu, L. Zhang, G. M. Mullen, G. Henkelman, and C. Buddie Mullins. Oxygen activation and reaction on PdAu bimetallic surfaces. *The Journal of Physical Chemistry C*, 119(21):11754–11762, 2015.

[28] A. Venugopal, J. Aluha, and M. S. Scurrell. The water-gas shift reaction over Au-based, bimetallic catalysts. the Au-M (M=Ag, Bi, Co, Cu, Mn, Ni, Pb, Ru, Sn, Tl) on Iron(iii) oxide system. *Catalysis Letters*, 90(1):1–6, 2003.

[29] T. Wang, B. Li, J. Yang, H. C., and L. Chen. First principles study of oxygen adsorption and dissociation on the Pd/Au surface alloys. *Phys. Chem. Chem. Phys.*, 13:7112–7120, 2011.

[30] W. Y. Yu, L. Zhang, G. M. Mullen, E. J. Evans, G. Henkelman, and C. B. Mullins. Effect of annealing in oxygen on alloy structures of Pd-Au bimetallic model catalysts. *Phys. Chem. Chem. Phys.*, 17:20588–20596, 2015.

[31] R. Todorovic and R.J. Meyer. A comparative density functional theory study of the direct synthesis of H_2O_2 on Pd, Pt and Au surfaces. *Catalysis Today*, 160(1):242 – 248, 2011. Heterogeneous catalysis by metals : New synthetic methods and characterization techniques for high reactivity.

[32] J. Gong. Structure and surface chemistry of gold-based model catalysts. *Chemical Reviews*, 112(5):2987–3054, 2012. PMID: 21524063.

[33] Jos L. C., Cordeiro M. Natlia D. S., and Gomes Jos R. B. A DFT study of the NO dissociation on gold surfaces doped with transition metals. *The Journal of Chemical Physics*, 138(7), 2013.

[34] K. Termentzidis and J. Hafner. CO adsorption on a Au/Ni(111) surface alloya DFT study. *Journal of Physics: Condensed Matter*, 19(24):246219, 2007.

[35] Jos L.C. Fajin, M. Natlia D.S. Cordeiro, and Jos R.B. Gomes. DFT study on the reaction of O_2 dissociation catalyzed by gold surfaces doped with transition metal atoms. *Applied Catalysis A: General*, 458:90 – 102, 2013.

[36] S. Liu, P. Jin, D. Zhang, C. Hao, and X. Yang. Reaction mechanism for methanol oxidation on Au(111): A density functional theory study. *Applied Surface Science*, 265:443 – 451, 2013.

[37] C. R. Chang, B. Long, X. F. Yang, and J. Li. Theoretical studies on the synergetic effects of aupd bimetallic catalysts in the selective oxidation of methanol. *The Journal of Physical Chemistry C*, 119(28):16072–16081, 2015.

[38] H. Jürgen, C. Wolverton, and G. Ceder. Toward computational materials design: The impact of density functional theory on materials research. *MRS Bulletin*, 31:659–668, 9 2006.

[39] S. Hao, W. Kam L., B. Moran, F. Vernerey, and G. B. Olson. Multi-scale constitutive model and computational framework for the design of ultra-high strength, high toughness steels. *Computer Methods in Applied Mechanics and Engineering*, 193(17,Äì20):1865 – 1908, 2004. Multiple Scale Methods for Nanoscale Mechanics and Materials.

[40] M. Sugihara, V. Buss, P. Entel, , and J. Hafner. The nature of the complex counterion of the chromophore in rhodopsin. *The Journal of Physical Chemistry B*, 108(11):3673–3680, 2004.

[41] L. J. Sham and W. Kohn. One-particle properties of an inhomogeneous interacting electron gas. *Phys. Rev.*, 145:561–567, May 1966.

[42] P. Hohenberg and W. Kohn. Inhomogeneous electron gas. *Phys. Rev.*, 136:B864–B871, Nov 1964.

[43] J. P. Perdew, K. Burke, and M. Ernzerhof. Generalized gradient approximation made simple. *Phys. Rev. Lett.*, 77:3865–3868, Oct 1996.

[44] K. Laasonen, R. Car, C. Lee, and David Vanderbilt. Implementation of ultrasoft pseudopotentials in *ab initio* molecular dynamics. *Phys. Rev. B*, 43:6796–6799, Mar 1991.

[45] P. Giannozzi, S. Baroni, N. Bonini, M. Calandra, R. Car, C. Cavazzoni, ..., and R. M. Wentzcovitch. QUANTUM ESPRESSO: a modular and open-source software project for quantum simulations of materials. *Journal of Physics: Condensed Matter*, 21(39):395502, 2009.

[46] M. L. Bellac. *Quantum Physics*. Cambridge University Press, The Edinburgh Building, Cambridge CB2 8RU, UK, 2006.

[47] W. Tang, E. Sanville, and G. Henkelman. A grid-based bader analysis algorithm without lattice bias. *Journal of Physics: Condensed Matter*, 21(8):084204, 2009.

[48] G. Henkelman, A. Arnaldsson, and H. Jonsson. A fast and robust algorithm for Bader decomposition of charge density. *Computational Materials Science*, 36(3):354 – 360, 2006.

[49] H. F. Rase. *Handbook of Commercial Catalysts: Heterogeneous Catalysts*. CRC Press, Corporate Blvd., Boca Raton. Aorida 33431, 2000.

[50] D. G. Pettifor. *Bonding and Structure of Molecules and Solids*. Clarendon Press, Oxford University Press, Walton Street, Oxford OX2 6DP, 1995.

[51] B. Hammer and J.K. Nørskov. Theoretical surface science and catalysis-calculations and concepts. In *Impact of Surface Science on Catalysis*, volume 45 of *Advances in Catalysis*, pages 71 – 129. Academic Press, 2000.

[52] H. Xin, A. Vojvodic, J. Voss, J. K. Nørskov, and A. P. Frank. Effects of d-band shape on the surface reactivity of transition-metal alloys. *Phys. Rev. B*, 89:115114, Mar 2014.